JEM Journal of Experimental Medicine

ARTICLE

Group 2 innate lymphoid cells support hematopoietic recovery under stress conditions

Takao Sudo[1,2,3], Yasutaka Motomura[2,4,5], Daisuke Okuzaki[6,7], Tetsuo Hasegawa[1], Takafumi Yokota[3], Junichi Kikuta[1,2,8], Tomoka Ao[1,8], Hiroki Mizuno[1,2], Takahiro Matsui[1,9], Daisuke Motooka[6,7], Ryosuke Yoshizawa[1], Takashi Nagasawa[2,10], Yuzuru Kanakura[3], Kazuyo Moro[2,4,5], and Masaru Ishii[1,2,8]

The cell-cycle status of hematopoietic stem and progenitor cells (HSPCs) becomes activated following chemotherapy-induced stress, promoting bone marrow (BM) regeneration; however, the underlying molecular mechanism remains elusive. Here we show that BM-resident group 2 innate lymphoid cells (ILC2s) support the recovery of HSPCs from 5-fluorouracil (5-FU)–induced stress by secreting granulocyte-macrophage colony-stimulating factor (GM-CSF). Mechanistically, IL-33 released from chemosensitive B cell progenitors activates MyD88-mediated secretion of GM-CSF in ILC2, suggesting the existence of a B cell–ILC2 axis for maintaining hematopoietic homeostasis. GM-CSF knockout mice treated with 5-FU showed severe loss of myeloid lineage cells, causing lethality, which was rescued by transferring BM ILC2s from wild-type mice. Further, the adoptive transfer of ILC2s to 5-FU–treated mice accelerates hematopoietic recovery, while the reduction of ILC2s results in the opposite effect. Thus, ILC2s may function by "sensing" the damaged BM spaces and subsequently support hematopoietic recovery under stress conditions.

Introduction

Hematopoietic stem cells (HSCs) and their progeny in the bone marrow (BM) perpetually generate numerous hematopoietic cells throughout our lifespan in steady-state and stressed conditions (Busch et al., 2015; Sun et al., 2014). In homeostatic conditions, HSCs are maintained and regulated in the specific microenvironment termed the "HSC niche," which is composed of various cell types (Decker et al., 2018; Ding et al., 2012; Qian et al., 2007; Sugiyama et al., 2006; Yamazaki et al., 2011). However, BM stress induced by chemotherapy or by total body irradiation (TBI) can cause various alterations in the BM environment, including reduction of hematopoietic cells, severe vascular regression, and increased cytokine production (Gaugler et al., 2001; Heissig et al., 2002; Hérault et al., 2017; Hooper et al., 2009), followed by metabolic fluctuation in hematopoietic stem and progenitor cells (HSPCs; Karigane et al., 2016). Consequently, HSPCs can initiate proliferation after BM injury (Venezia et al., 2004; Wilson et al., 2008). Additionally, during HSC transplantation, recipients usually undergo myeloablative conditioning therapy to achieve efficient engraftment (Tomita et al., 1994). Hence, stressed BM environments might induce BM recovery (Hérault et al., 2017; Tikhonova et al., 2019).

Group 2 innate lymphoid cells (ILC2s) functionally mirror T helper type 2 cells. However, they have completely different activation triggers. In response to exposure to cytokines, such as IL-25 or IL-33, ILC2s produce type 2 cytokines (Moro et al., 2010; Vivier et al., 2018). ILC2s exist in a variety of peripheral tissues as tissue-resident cells (Gasteiger et al., 2015) and are involved in the pathogenesis of allergies, innate immune response to extracellular parasites, and tissue repair (Bartemes et al., 2012; Monticelli et al., 2015; Neill et al., 2010). In addition, recent studies have shown that type 2 cytokine production by multiple differentiated cells, including ILC2s, results in in situ hematopoiesis, contributing to host protection after helminth infection (Hui et al., 2015; Inclan-Rico et al., 2020). Although ILC2 lineages

[1]Department of Immunology and Cell Biology, Graduate School of Medicine and Frontier Biosciences, Osaka University, Osaka, Japan; [2]World Premier International Research Center Initiative Immunology Frontier Research Center, Osaka University, Osaka, Japan; [3]Department of Hematology and Oncology, Osaka University Graduate School of Medicine, Osaka, Japan; [4]Laboratory for Innate Immune Systems, Department of Microbiology and Immunology, Graduate School of Medicine, Osaka University, Osaka, Japan; [5]Laboratory for Innate Immune Systems, RIKEN Center for Integrative Medical Sciences, Kanagawa, Japan; [6]Single Cell Genomics, Human Immunology, World Premier International Research Center Initiative Immunology Frontier Research Center, Osaka University, Osaka, Japan; [7]Genome Information Research Center, Research Institute for Microbial Diseases, Osaka University, Osaka, Japan; [8]Laboratory of Bioimaging and Drug Discovery, National Institutes of Biomedical Innovation, Health and Nutrition, Osaka, Japan; [9]Department of Pathology, Osaka University Graduate School of Medicine, Osaka, Japan; [10]Laboratory of Stem Cell Biology and Developmental Immunology, Graduate School of Medicine and Frontier Biosciences, Osaka University, Osaka, Japan.

Correspondence to Masaru Ishii: mishii@icb.med.osaka-u.ac.jp.

exist in the BM, previously referred to as the ILC2 progenitor, they produce low amounts of IL-5 (Hoyler et al., 2012). It has been shown that early and final differentiation of ILC2s occur in the fetal liver and peripheral tissues, respectively (Koga et al., 2018). Additionally, parabiosis studies have shown that ILC2s in BM are not the source of ILC2s in peripheral tissues (Gasteiger et al., 2015), suggesting that the ILC2s in BM are tissue resident, and are expected to have a BM-specific role. However, how BM-resident ILC2s become mature or what the function of ILC2s in the BM is remain largely unknown.

Our goal in this study is to elucidate the key signals transmitted from stressed BM environments. Although several signals have been reported to be involved in stress hematopoiesis during treatment with 5-fluorouracil (5-FU; Hérault et al., 2017; Tikhonova et al., 2019; Zhao et al., 2014), the critical trigger mechanisms occurring in the early stage have not been fully elucidated, in part due to the phenotypic changes caused in HSPCs following acute BM stress, including down-regulation of c-Kit (Randall and Weissman, 1997; Sudo et al., 2012), which makes it difficult to purify these cells from stressed BM. Further, it would be challenging to clearly decipher whether the altered gene expression in HSPCs following BM stress is caused by cell-extrinsic or -intrinsic factors. To overcome these challenges, in this study, we conducted a comprehensive RNA sequencing (RNA-seq) analysis of HSPCs that had been transplanted into injured BM after BM stress. This approach allowed us to identify essential proliferative and anti-apoptotic signals supplied from the damaged BM environment toward HSPCs as early as 2 d after BM injury.

Here, we demonstrate a novel regulatory mechanism where BM-resident ILC2s support hematopoietic recovery from 5-FU–induced stress through secretion of GM-CSF. In addition, we found that IL-33 released from chemo-sensitive B cell progenitors activates MyD88-mediated secretion of GM-CSF in ILC2s. Together, we clarify the essential mechanism of hematopoietic recovery after BM injury. This should promote the development of an ex vivo HSC amplification method and adjunct therapy against chemoradiotherapy-induced neutropenia and improved engraftment.

Results

Myelosuppressive BM environments influence the behavior of HSPCs

We first visualized the physiological BM to evaluate the spatiotemporal properties of transplanted HSPCs within a stressed environment niche (Lo Celso et al., 2009). To achieve this, lineage (Lin)$^-$stem cell antigen-1 (Sca1)$^+$c-Kit^{Hi} (LSK) cells, an HSPC-enriched fraction, sorted from WT mice and labeled with green dye 5-chloromethylfluorescein diacetate (CMFDA), were transplanted into steady-state (control) or conditioned mice treated with 5-FU 2 d before transplantation. On the day following transplantation, we performed time-lapse imaging of the skull BM in recipient mice (Fig. S1, A and B). Transplanted HSPCs were visualized in both untreated and 5-FU–treated recipient mice with similar frequency per 10^5 transplanted LSK cells (Fig. S1 C). Nevertheless, HSPCs transplanted into 5-FU–treated recipients showed significantly lower speed or displacement compared with those transplanted into control recipients (Fig. S1, D–F; Video 1; and Video 2). We also evaluated the distances between each HSPC and endothelial cells (ECs), and found that the mean distance was shorter in 5-FU–treated mice than in control mice (Fig. S1 G). Further, of the HSPCs transplanted into 5-FU–treated mice, 64% (23 out of 36) were persistently adhering to ECs during time-lapse imaging, which was higher than in the control condition (26%; Fig. S1 G). These variable findings in the behavior of HSPCs depending on the environment motivated us to seek stress-related signals provided to HSPCs.

HSPCs in stressed BM receive strong GM-CSF signals

Next, we conducted a comprehensive RNA-seq analysis of HSPCs from cytomegalovirus-actin-globin (CAG)–enhanced GFP (EGFP) mice that had homed into recipient BM treated with or without 5-FU (Fig. 1 A). The direct effect of the remaining 5-FU against transplanted HSPCs could be negligible as 5-FU is rapidly metabolized (Fraile et al., 1980). The majority of EGFP$^+$ cells that had homed in to both groups were included in Lin$^-$Sca1$^+$c-Kit$^+$ fraction (Fig. 1 B). Comprehensive RNA-seq analysis of sorted EGFP$^+$ cells revealed that 1,130 genes were differentially expressed between the two groups, including 641 up-regulated genes and 489 down-regulated genes. Among them, cell cycle–promoting genes, including cyclin (CCN) B1 (*Ccnb1*), *Ccna2*, *Ccne2*, CCN-dependent kinase 1 (*Cdk1*), and *Cdk4*, were significantly up-regulated in HSPCs transplanted into 5-FU–treated recipients (Fig. 1 C). Downstream effects analysis based on the Ingenuity Pathway Analysis software revealed that biological functional categories "cell cycle" and "cellular growth and proliferation" were activated, whereas "cell death" was suppressed in HSPCs transplanted into 5-FU–treated recipients (Fig. S2, A–C). Next, we conducted an upstream analysis to identify upstream regulators responsible for HSPC activation in stressed BM conditions. Cellular growth–promoting transcriptional regulators, including *Myc*, *Ccnd1*, *E2f1*, and *Foxm1*, were significantly activated. In contrast, cellular growth–inhibitory regulators, including *Cdkn2a*, *p53*, and *Rb1*, were significantly inhibited in HSPCs from 5-FU–treated recipients (Fig. S2, D and E). These results suggest that HSPCs lodged in BM receive proliferative signals from 5-FU–treated microenvironments, followed by up-regulation of genes involved in cell cycle activation and cellular proliferation. Moreover, we found that signals from colony-stimulating factor 2 (CSF2/GM-CSF), hepatocyte growth factor (HGF), vascular endothelial growth factor (VEGF), and angiopoietin-2 (ANGPT2), at the top of the hierarchy in upstream pathways, were significantly activated in HSPCs that were transplanted into 5-FU–treated mice (Fig. S2 F). We conducted quantitative RT-PCR (qRT-PCR) to evaluate gene expression levels of growth factors in total BM cells or ECs in BM on day 0 (control) and day 2 after 5-FU treatment. Notably, the level of *Csf2*, encoding GM-CSF, was highly increased in total BM cells after 5-FU treatment compared with that of the control (Fig. 1 D). The level of *Hgf* was slightly increased in total BM cells after 5-FU treatment, whereas *Csf2* and *Hgf* were not expressed in ECs. In contrast, ECs expressed higher levels of

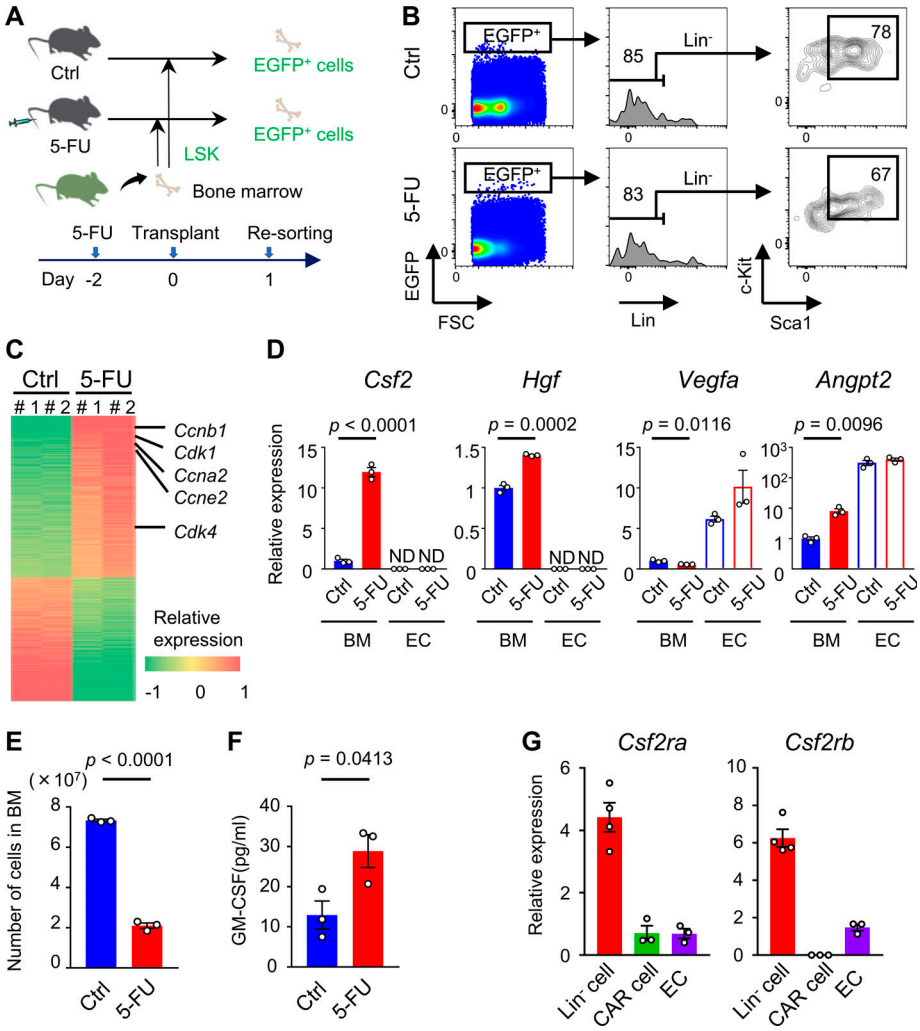

Figure 1. **HSPCs in stressed BM receive strong GM-CSF signals. (A–C)** LSK cells, which were sorted from CAG-EGFP mice, were transplanted into steady-state control (Ctrl) or 5-FU–treated WT mice. Then, EGFP⁺ cells in the recipient BM were sorted from two groups, and RNA-seq analyses were conducted. **(A)** Schematic of the procedure. **(B)** Flow cytometry plots of BMMNCs of untreated (control) or 5-FU–treated recipient WT mice that were transplanted with LSK cells from CAG-EGFP mice. Results shown are representative of two independent experiments. **(C)** Heat map of differentially expressed genes in RNA-seq analyses of HSPCs transplanted and homed into recipient BM (5-FU versus control); *n* = 2 per group. **(D–F)** Phenotypical changes of WT mice through a single 5-FU (200 mg/kg) injection. Each experiment was performed on day 0 (control) and day 2. **(D)** qRT-PCR analyses for the expression of indicated genes of total BM cells and ECs; *n* = 3, representative of two independent experiments. **(E)** The numbers of total BM cells in femurs and tibias; *n* = 3, representative of two independent experiments. **(F)** GM-CSF protein levels in femur analyzed by ELISA; *n* = 3, representative of two independent experiments. **(G)** qRT-PCR analyses for the expression of *Csf2ra* and *Csf2rb* genes in Lin⁻ cells, CAR cells, and ECs that were collected from BM of WT mice 2 d following 200 mg/kg 5-FU injection; *n* = 3 or 4, representative of two independent experiments. In the bar charts, the results are shown as mean ± SEM, and each dot represents an individual mouse. Statistical significance was determined by unpaired Student's *t* test. ND, not detectable.

Vegfa and *Angpt2* compared with total BM cells, although there was no statistical difference in expression of these markers between 5-FU–treated and control ECs (Fig. 1 D). Collectively, these results indicate that HSPCs receive proliferative and anti-apoptotic signals from injured BM environments.

Among the four growth factors extracted from upstream analysis, we focused on CSF2/GM-CSF as a possible key signal for hematopoietic recovery because it has the highest *z*-score with highest significance (Fig. S2 F), and the degree of up-regulation in 5-FU–treated BM cells was the highest (Fig. 1 D). We collated our RNA-seq bioset with another one (GSE #32986), in which fluctuations in the gene expression profiles of dendritic cells induced by GM-CSF stimuli in vitro were analyzed (Min et al., 2012). A strong positive correlation was observed between the two biosets (Fig. S2 G). This result supports the theory that GM-CSF directly stimulates HSPCs in 5-FU–treated mice. Indeed, ELISA revealed that GM-CSF protein in the BM was increased in response to 5-FU treatment, whereas the number of BM cells was decreased (Fig. 1, E and F). Nevertheless, GM-CSF protein in serum was undetectable on both day 0 and day 2 after 5-FU treatment (data not shown). We also conducted qRT-PCR analyses of CXCL12-abundant reticular (CAR) cells, a type of HSC niche component in BM (Sugiyama et al., 2006); however, *Csf2* expression was not detected before or after 5-FU treatment (data not shown). Murine GM-CSF receptors, encoded by *Csf2ra* and *Csf2rb*, are expressed in HSPCs and more committed progenitors

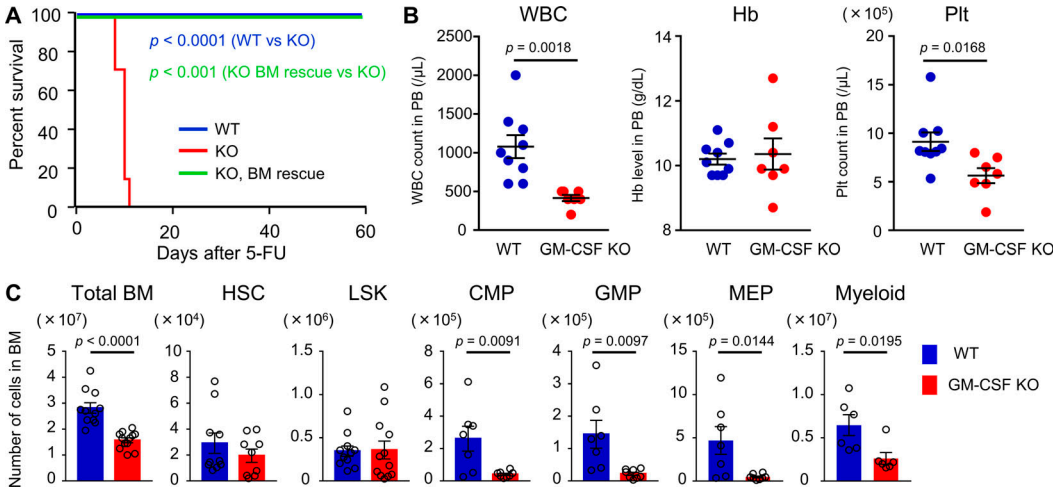

Figure 2. **GM-CSF is crucial for BM recovery. (A)** Kaplan–Meier survival curves. WT (blue line, *n* = 10) or GM-CSF–KO mice (red line, *n* = 7) were treated with a single dose of 200 mg/kg 5-FU. In the BM rescue group, KO mice were treated with 5-FU, and 2 d later, they were transplanted with 1 × 10^7 BM cells from WT mice treated with 200 mg/kg 5-FU 2 d prior (green line, *n* = 6). Data are pooled from two independent experiments. **(B and C)** WT and GM-CSF–KO mice were treated with 150 mg/kg 5-FU. PB counts and BM cellularity were analyzed on day 8. **(B)** WBC, hemoglobin (Hb), and platelet (Plt) counts in PB; *n* = 9 in WT, *n* = 7 in KO. Data are pooled from two independent experiments. **(C)** The numbers of total BM cells, HSCs (CD48$^-$CD150$^+$ LSK cells), LSK cells, CMPs, GMPs, MEPs, and Gr1$^+$ or CD11b$^+$ myeloid cells from femurs and tibias; *n* = 6–12, pooled from two independent experiments. In the bar charts, the results are shown as mean ± SEM, and each dot represents an individual mouse. Statistical significance was determined by the log-rank test (A) or unpaired Student's *t* test (B and C).

(Seita et al., 2012). While both genes were highly expressed in Lin$^-$ cells after 5-FU treatment, the levels were lower in CAR cells and ECs (Fig. 1 G). These results indicate that high amounts of GM-CSF produced by BM cells stimulate HSPCs or progenitors, which express high levels of GM-CSF receptors in 5-FU–treated BM environments.

GM-CSF is crucial for BM recovery

To elucidate the functional importance of GM-CSF in hematopoietic recovery, we used GM-CSF–KO mice. This line was reported to show no major perturbation of hematopoiesis (Dranoff et al., 1994; Stanley et al., 1994). We also confirmed that blood cell counts and the numbers of total BM cells, long-term HSCs (CD48$^-$CD150$^+$ LSK cells), LSK cells, common myeloid progenitors (CMPs), granulocyte-macrophage progenitors (GMPs), megakaryocyte-erythroid progenitors (MEPs), and Gr1$^+$ or CD11b$^+$ myeloid cells in the BM in GM-CSF–KO mice were not less than those in WT mice (Fig. S3, A and B). BrdU incorporation in LSK cells was similar between WT and GM-CSF–KO mice (Fig. S3 C). Thus, GM-CSF is not required for homeostatic hematopoiesis. However, Kaplan–Meier survival curve analysis comparing the survival rate in WT and GM-CSF–KO mice after 200 mg/kg 5-FU injection showed that while all WT mice survived, all KO mice died. Interestingly, 5-FU–treated KO mice that had been transplanted with BM cells from WT mice were completely rescued (Fig. 2 A). To rule out death caused by pulmonary dysfunction that is found in GM-CSF–KO mice (Dranoff et al., 1994), we evaluated the pathology of the lungs in mutant mice after 5-FU treatment. Severe pathological changes were not observed in the lung of GM-CSF–KO mice, although there was a small tubercule composed of eosinophilic protein, consistent with the previous report (Fig. S3, D and E; Dranoff et al., 1994). These results indicated that the cause of death in these mice was BM failure. We next evaluated hematopoietic recovery in WT and KO mice on day 8 after 150 mg/kg 5-FU injection, in which lethality due to GM-CSF deficiency could be avoided. As a result, KO mice showed significantly reduced numbers of white blood cells (WBCs) and platelets in peripheral blood (PB) compared with those in WT mice (Fig. 2 B). The numbers of total BM cells, CMPs, GMPs, MEPs, and myeloid cells were significantly reduced in GM-CSF–KO mice, suggesting that GM-CSF is necessary for myeloid differentiation from HSCs or multipotent progenitors during hematopoietic recovery (Fig. 2 C). We further found that 5.5 Gy of TBI could be lethal for GM-CSF–KO mice, while WT mice exposed to the same dose of irradiation were not killed (Fig. S3 F). These results demonstrate that GM-CSF is required for normal hematopoietic recovery following BM stress.

BM ILC2s produce GM-CSF after BM stress

Although previous reports have shown that GM-CSF is produced by a variety of cell types including T lymphocytes upon stimulation with LPS, IL-1, IL-6, and TNF-α (Bagby et al., 1986; Lukens et al., 2012; Thorens et al., 1987), which type of cells is responsible for secreting GM-CSF in stressed condition remained unknown. To search for the specific cellular populations that produce GM-CSF, we analyzed cell surface markers on GM-CSF$^+$ cells that were collected from BM treated with 5-FU. We found that all of GM-CSF$^+$ cells expressed CD45, and notably, a majority of them expressed Sca1, whereas the expression levels of CD4, CD8, CD19, and CD11c were low or negative (Fig. 3 A). We also found that Sca1$^+$ BM cells at 5-FU day 2 expressed higher levels of *Csf2* compared with total BM cells (Fig. 3 B). Therefore, we sorted Sca1$^+$ cells from BM mononuclear cells (BMMNCs) isolated from 5-FU–treated mice and performed single-cell RNA-seq analysis. Further, t-distributed stochastic neighbor embedding

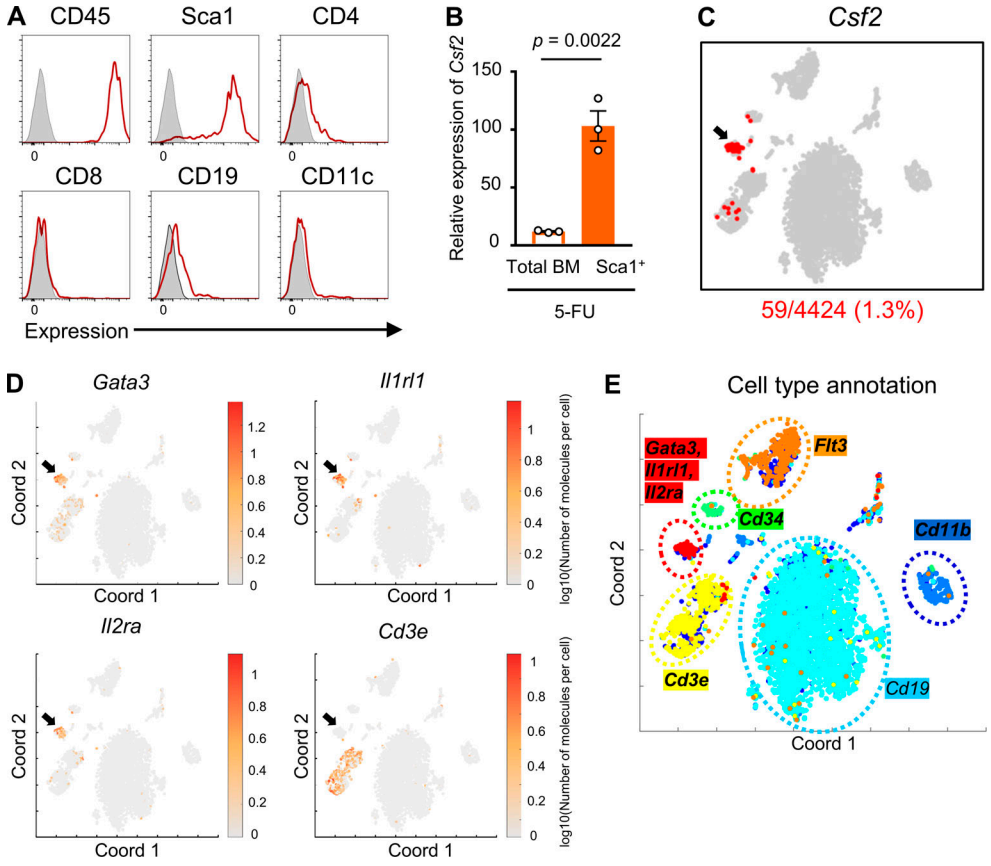

Figure 3. **The BM *Csf2*-positive cluster is composed of ILC2s. (A)** Histograms of surface markers in GM-CSF⁺ BM cells from 5-FU–treated WT mice. The tinted lines show the background level. Results shown are representative of two independent experiments. **(B)** qRT-PCR analyses for the expression of *Csf2* in total BM cells and Sca1⁺ BM cells from 5-FU–treated mice; $n = 3$, representative of two independent experiments. Bars indicate expression level relative to that in total BM cells at day 0. **(C–E)** Single-cell RNA-seq analysis of Sca1⁺ BMMNCs sorted from 5-FU–treated WT mice. **(C)** t-SNE projection highlighting *Csf2* expressing cells (number of detected mRNA molecules >0). The arrow shows a cluster expressing *Csf2*. **(D)** t-SNE projection of the expression pattern for *Gata3*, *Il1rl1*, *Il2ra*, and *Cd3e*. The color of each cell represents the $\log_{10}$(number of molecules per cell). The arrows are in the same position as in C. **(E)** Six main clusters generated by t-SNE analysis. Each cluster expressed *Cd11b*, *Cd19*, *Cd34*, *Cd3e*, *Flt3*, and a combination of *Gata3*, *Il1rl1*, and *Il2ra*. For the 5-FU–treated mice groups, mice were injected intravenously with 200 mg/kg 5-FU 2 d before being euthanized (A–E). Results are shown as mean ± SEM, and each dot represents an individual mouse. Statistical significance was determined by unpaired Student's *t* test (B). Coord, t-SNE coordinate.

(t-SNE) analysis highlighted a specific cluster expressing *Csf2* (Fig. 3 C). This cluster was characterized by high expression levels of *Gata3*, *Il1rl1*, *Il2ra*, and type-2 cytokine genes, such as *Il5* and *Il13*, and negative expression of *Cd3*e, which corresponds to the characteristic gene expression pattern of ILC2s (Fig. 3, D and E; and Table S1; Vivier et al., 2018). Additionally, an annotation study of *Csf2*⁺ cells highlighted the coexpression of genes, including *Il2ra*, *Gata3*, and *Il1rl1*, suggesting that among hematopoietic cells, BM ILC2s express higher levels of *Csf2* (Table S2). The finding that ILC2s express Sca1 (Moro et al., 2010) would partially explain why GM-CSF⁺ cells expressed Sca1 (Fig. 3 A). Consistently, it was reported that ILC2s have a high productive capacity of GM-CSF in response to active stimulation (Moro et al., 2010; Neill et al., 2010). We identified Lin⁻CD25⁺IL-7Rα⁺IL-33R⁺ ILC2s among BM cells (Fig. 4 A); in response to 5-FU treatment, the proportion of ILC2s increased, compared with those in untreated condition (Fig. 4 B). Consequently, the number of ILC2s did not decrease, although BM cellularity dropped after 5-FU treatment (Fig. 4 C). In addition, ILC2s of 5-FU–treated mice exhibited increased forward (FSC) and side scatter characteristics (SSC; Fig. 4 D). They showed up-regulation of activation markers, such as programmed cell death-1 (PD-1), IL-33R, and CD25, and down-regulation of IL-7Rα (Fig. 4 D), indicating that ILC2s become activated in response to 5-FU treatment (Li et al., 2017; Yu et al., 2016). Next, we performed a qRT-PCR analysis to evaluate the expression of *Csf2* in BM immune cells. In the homeostatic control condition, T lymphocytes expressed sixfold higher levels of *Csf2* compared with whole BM cells, whereas B lymphocytes, monocytes, and neutrophils expressed much lower levels. In contrast, ILC2s expressed much higher levels of *Csf2* than other populations, while in the 5-FU–treated ILC2s, *Csf2* levels increased further (Fig. 4 E). Flow-cytometric analysis to detect intracellular GM-CSF revealed that a Lin⁻IL-33R⁺ ILC2-enriched population of 5-FU–treated mice partially expressed GM-CSF, whereas the same population of control mice did not (Fig. 4 F). We further found that the TBI for WT mice also up-regulated the *Csf2* level in BM ILC2s (Fig. S3 G). These results strongly suggest that BM ILC2s in vivo up-regulate *Csf2* and begin to produce high levels of GM-CSF upon BM stress.

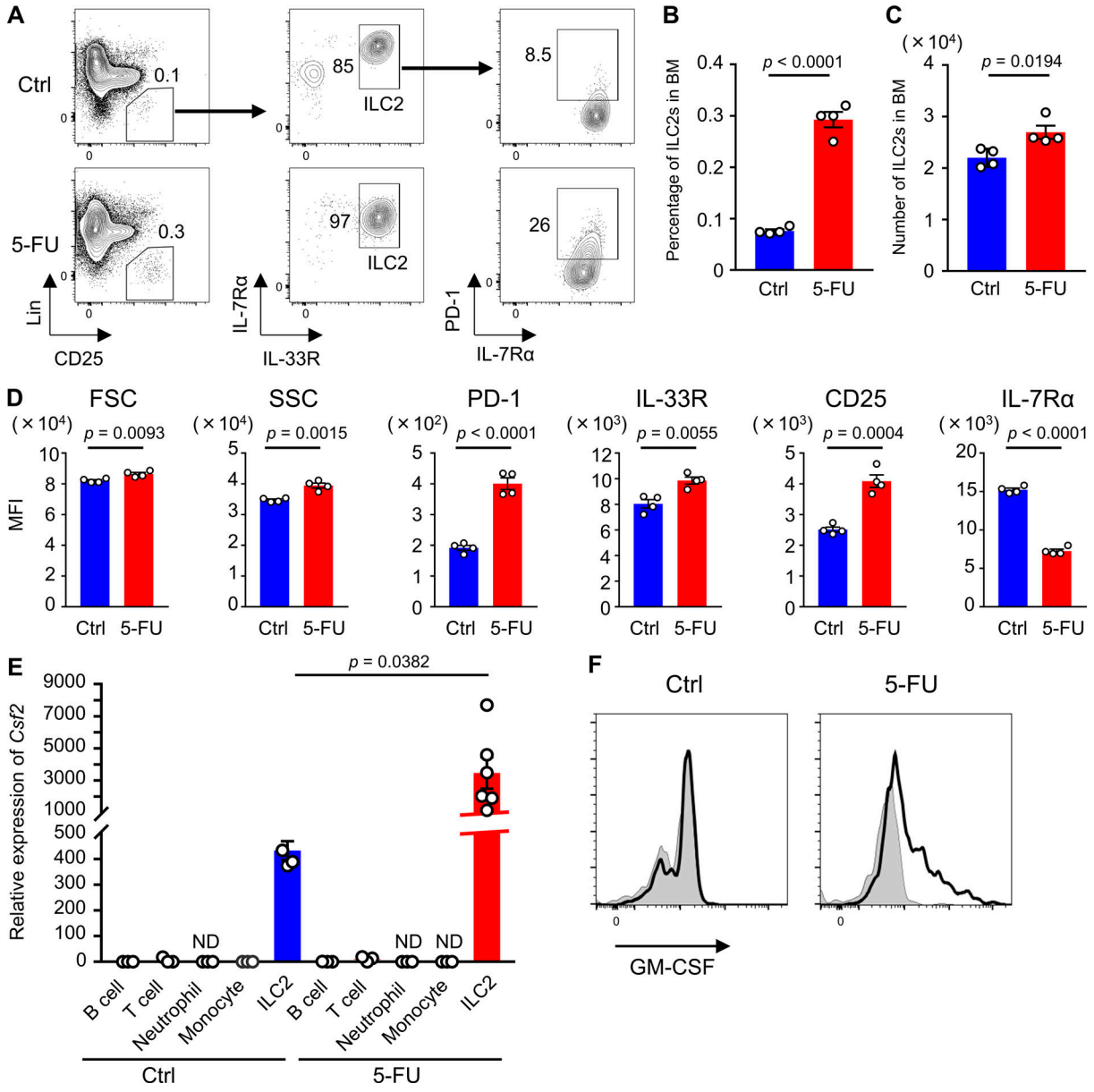

Figure 4. **BM ILC2s become activated and produce GM-CSF after BM stress. (A)** Representative flow cytometry plots of BM cells to identify Lin⁻CD25⁺IL-7Rα⁺IL-33R⁺ ILC2s. **(B)** Percentage of ILC2s among BMMNCs; *n* = 4, representative of two independent experiments. **(C)** Number of ILC2s in femurs and tibias; *n* = 4, representative of two independent experiments. **(D)** Mean fluorescence intensity (MFI) of markers in ILC2 population; *n* = 4, representative of two independent experiments. **(E)** qRT-PCR analyses for the expression of *Csf2* in B cells, T cells, neutrophils, monocytes, and ILC2s; *n* = 3–6, representative of two independent experiments. Bars indicate expression level relative to that in total BM cells at day 0. **(F)** Intracellular GM-CSF levels in Lin⁻IL-33R⁺ population. The tinted lines show the background levels. Results shown are representative of two independent experiments. For the 5-FU–treated mice groups, mice were injected intravenously with 200 mg/kg 5-FU 2 d before being euthanized (A–F). In the bar charts, results are shown as mean ± SEM, and each dot represents an individual mouse. Statistical significance was determined between the control (Ctrl) and 5-FU–treated mice by unpaired Student's *t* test (B–E). ND, not detectable.

IL-33–ST2–MyD88 axis promotes up-regulation of *Csf2*

The aforementioned results showed that BM ILC2s promote recovery after stress by producing GM-CSF; however, the question regarding the up-regulation mechanism of *Csf2* in vivo remains elusive. It has been reported that alarmins such as IL-1 family members, released by injured cells, are increased in BM after irradiation or 5-FU injection (Huang et al., 2019; Pietras et al., 2016). IL-33, a member of the IL-1 family, is released from cells upon cellular damage (Lüthi et al., 2009). Additionally, it has been shown that cultured ILC2s become activated and produce type 2 cytokines including GM-CSF in response to IL-33 in vitro (Brickshawana et al., 2011; Hoyler et al., 2012), prompting us to analyze the expression of IL-33 in BM. Although ECs constitute a major source of IL-33 in some tissues (Moussion et al., 2008), our flow-cytometric analysis of IL-33–GFP mice showed that the IL-33 level in BM ECs was low (Fig. S4 A). Consistent with previous reports, the analysis of flushed BM samples revealed that IL-33 was expressed on B cell progenitors,

such as pro-B, pre-B, and immature B cells, among hematopoietic cells (Fig. 5, A and B; Rana et al., 2019; Stier et al., 2019). We also conducted a qRT-PCR analysis of BM cells from WT mice and found that CD19$^+$ cells expressed higher levels of *Il33* than stromal cells or ECs (Fig. 5 C). The numbers of B cell progenitors, mainly residing within CD45^{Lo} fraction in BM, dramatically decreased after 5-FU, indicating that these cells were easily damaged by 5-FU (Fig. 5, D and E; and Fig. S4 B). As expected, the IL-33 protein level in BM supernatant was significantly increased after 5-FU treatment (Fig. 5 F). Additionally, supernatant from the culture medium of CD19$^+$ cells contained IL-33 after incubation with 5-FU (Fig. S4 C). Immunohistochemical staining of a 5-FU–treated BM section showed that a majority of the IL-33$^+$ cells also expressed CD19 (Fig. S4 D). These results indicate that B cell progenitors are the major source of IL-33 in BM after 5-FU treatment. Next, we performed qRT-PCR analysis using IL-33$^{GFP/GFP}$ (IL-33 deficient) mice and found that *Csf2* was suppressed in 5-FU–treated mutant ILC2s (Fig. 5 G). Unlike the GM-CSF–KO mice, the IL-33$^{GFP/GFP}$ mice survived the 5-FU treatment (data not shown); however, the numbers of myeloid progenitors in IL-33$^{GFP/GFP}$ mice decreased compared with those in the WT mice (Fig. S4 E). From these results, we concluded that IL-33, released primarily from B cell progenitors in response to 5-FU injection, is correlated with *Csf2* up-regulation in ILC2s.

MyD88 is the key adaptor protein for inflammatory signaling pathways downstream of the IL-1 receptor family members as well as TLRs (Dinarello, 2018). In addition, it has been reported that TLR ligands control GM-CSF production by synovial ILC2s (Hirota et al., 2018). Based on these reports, we used MyD88-KO mice to assess the functional importance of this molecule for BM recovery. The expression level of *Csf2* was dramatically suppressed in BM ILC2s obtained from 5-FU–treated MyD88-KO mice compared with those from WT mice, although there was no difference between the two groups under homeostatic conditions (Fig. 6 A). MyD88-KO mice injected with 200 mg/kg 5-FU showed a marked reduction in survival; five out of nine KO mice died (Fig. 6 B). Additionally, the numbers of myeloid progenitors were significantly reduced in MyD88-KO mice compared with those in the WT mice after 5-FU treatment (Fig. 6 C). These results suggested that MyD88 is involved in up-regulation of *Csf2* in ILC2s and myeloid recovery after BM injury.

Adoptive transfer of ILC2s possesses therapeutic potential for myelosuppressive animals

To assess the contribution of ILC2s to BM recovery, we neutralized ILC2s by treating the WT mice with anti-CD90.2 antibody (Ab). After confirming that an intraperitoneal injection of 200 µg anti-CD90.2 Ab every other day, for four times, effectively reduced ILC2s in BM (Fig. S5 A), the BM recovery of these mice on day 8 after 5-FU treatment was assessed. The numbers of myeloid progenitors were significantly reduced in Ab-treated mice compared with those in the control mice (Fig. S5 B). Although this Ab also targets CD90.2$^+$ cells, including T lymphocytes, the effect of T cell depletion against GM-CSF production was thought to be limited; the expression level of *Csf2* in T cells was much lower than ILC2s (Fig. 4 E). Thus, depletion of CD90.2$^+$ cells, including ILC2s, by injection of anti-CD90.2 Ab impaired BM regeneration. Next, to determine the therapeutic potential of ILC2s for hematopoiesis, we evaluated whether the hematopoietic recovery could be accelerated by the adoptive transfer of ILC2s. Sorted BM ILC2s were cultured in medium supplemented with IL-2 and IL-7 to expand cell number, and 2 × 10^5 cells were transferred intravenously on days 1 and 2 after 5-FU injection (Fig. 7 A). Flow-cytometric analysis revealed that cultured cells kept the CD25$^+$IL-33R$^+$ phenotype (Fig. S5 C). We confirmed that the grafts had successfully lodged in the BM of the recipient mice by detecting transferred ILC2s from CAG-EGFP mice using in vivo imaging and flow cytometry (Fig. 7, B and C). We analyzed whether the transfer of ILC2s accelerated the recovery of hematopoietic cells on day 7 after 5-FU treatment (150 mg/kg); inversive production of myeloid progenitors was not yet observed at that time under normal process (Hérault et al., 2017). WT mice that were transferred with ILC2s from WT mice showed significantly increased numbers of LSK cells, myeloid progenitors, and differentiated myeloid cells in the BM than those in control mice, while those transferred with ILC2s from GM-CSF–KO did not (Fig. 7, D–F). However, transfer of ILC2s from WT or GM-CSF–KO mice did not significantly increase the PB WBC count in WT recipients (Fig. 7 G). Since it is possible that transferred ILC2s increased hematopoietic cells through the recovery of stromal niche cells, we evaluated the proportion of CAR cells relative to BM space in CXCL12-GFP mice that were transferred with ILC2s from WT mice after 5-FU treatment. There was no significant difference in the GFP$^+$ area between control and ILC2-transferred mice (Fig. S5, D and E). These data suggested that transferred ILC2s secreting GM-CSF in situ in 5-FU–treated BM acted mainly on hematopoietic cells, rather than stromal cells. Finally, we evaluated the rate of hematopoietic recovery in GM-CSF–KO mice after transferring ILC2s. While the transfer of ILC2s from WT mice significantly increased LSK cells, myeloid progenitors, and differentiated myeloid cells in the BM, and the WBC counts in PB in 5-FU–treated GM-CSF–KO mice compared with those in the control condition, grafts from GM-CSF–KO or MyD88-KO mice did not induce significant recovery (Fig. 8, A–D). We also challenged the improved survival of GM-CSF–KO mice after treatment with 200 mg/kg 5-FU by transferring ILC2s from WT mice. Survival analysis showed that all recipients in the rescue group were alive after day 60, whereas all mice in the control group died (Fig. 8 E). Collectively, these findings suggested that the adoptive transfer of ILC2s resulted in various levels of faster recovery during the process of myeloid differentiation, meaning that it might have therapeutic potential in myelosuppressive animals.

Discussion

In this study, we identified BM ILC2s upon BM stress secreting a high amount of GM-CSF and revealed that the IL-33–ST2–MyD88 axis is important for the up-regulation of *Csf2* in BM ILC2s, proposing a novel mechanism where BM ILC2s control hematopoietic recovery by monitoring BM injury and producing GM-CSF. Several studies have shown that mature or immature hematopoietic cells, including megakaryocytes and granulocytes, promote hematopoietic

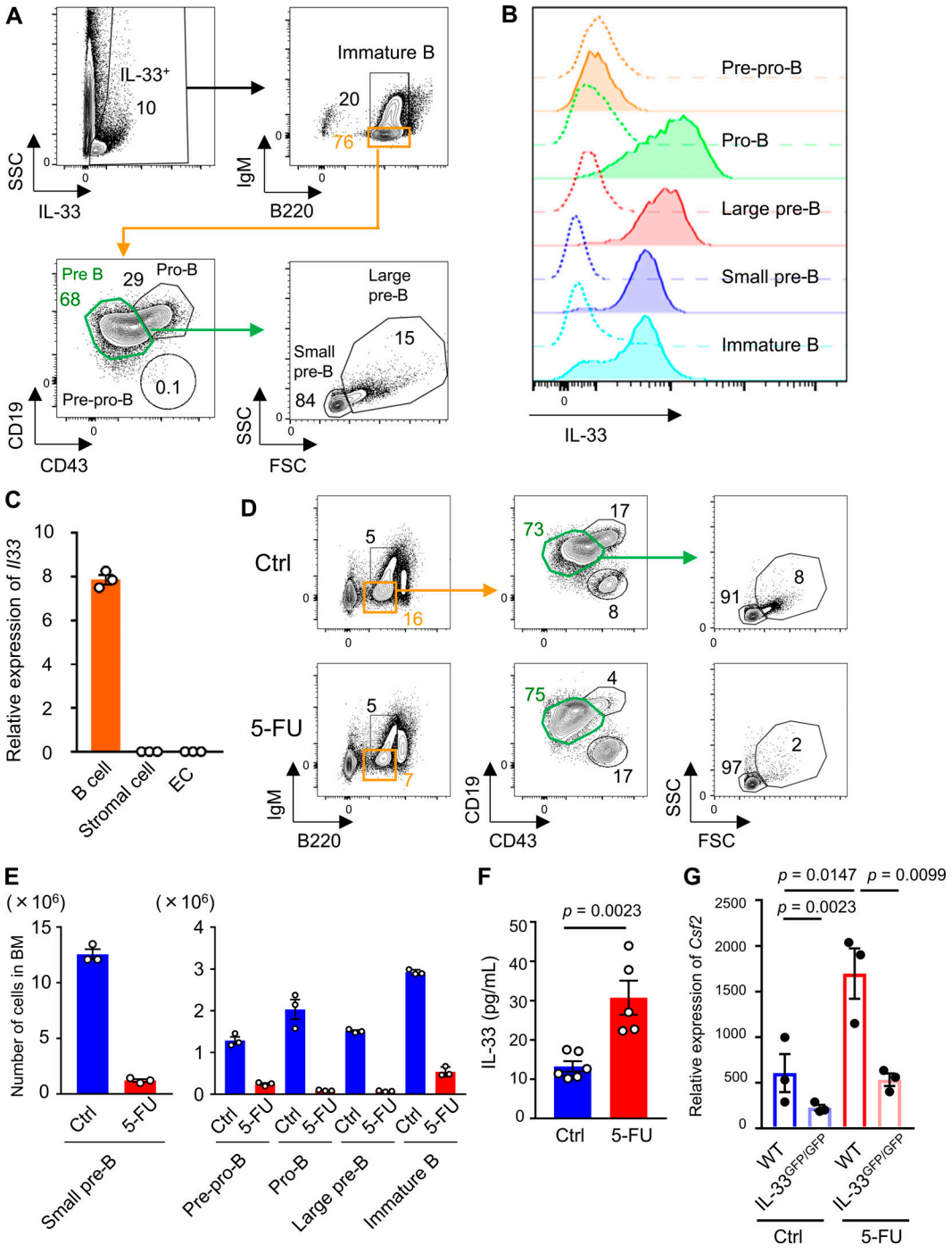

Figure 5. **IL-33 secreted by B cell progenitors activates BM ILC2s after 5-FU treatment. (A)** Flow cytometry of BM cells from IL-33–GFP mice showing B cell progenitors, including pre-pro-B, pro-B, large pre-B, small pre-B, and immature B cells. Each number indicates the percentage of each fraction. Results shown are representative of three independent experiments. **(B)** IL-33–GFP levels in each B cell progenitor fraction of IL-33–GFP mice. Dashed lines represent background levels in WT mice. Results shown are representative of three independent experiments. **(C)** qRT-PCR analyses for the expression of *Il33* in $CD19^+$ B cells, stromal cells, and ECs sorted from WT mice; $n = 3$, representative of two independent experiments. **(D)** Flow cytometry plots of BM cells from control (Ctrl) or 5-FU–treated WT mice to evaluate the size of each B cell progenitor. Results shown are representative of three independent experiments. **(E)** The numbers of each B cell progenitor fraction from femurs and tibias of control or 5-FU–treated WT mice; $n = 3$, representative of two independent experiments. **(F)** IL-33 protein levels in femur analyzed by ELISA; $n = 6$ in control, $n = 5$ in 5-FU, representative of two independent experiments. **(G)** qRT-PCR analyses for the expression of *Csf2* in BM ILC2s from WT and $IL\text{-}33^{GFP/GFP}$ mice; $n = 3$, representative of two independent experiments. In 5-FU–treated groups, mice were intravenously injected with 200 mg/kg 5-FU 2 d before euthanization. Results are shown as mean ± SEM. Statistical significance was determined by unpaired Student's *t* test (F) or ANOVA with the Bonferroni post hoc test (G).

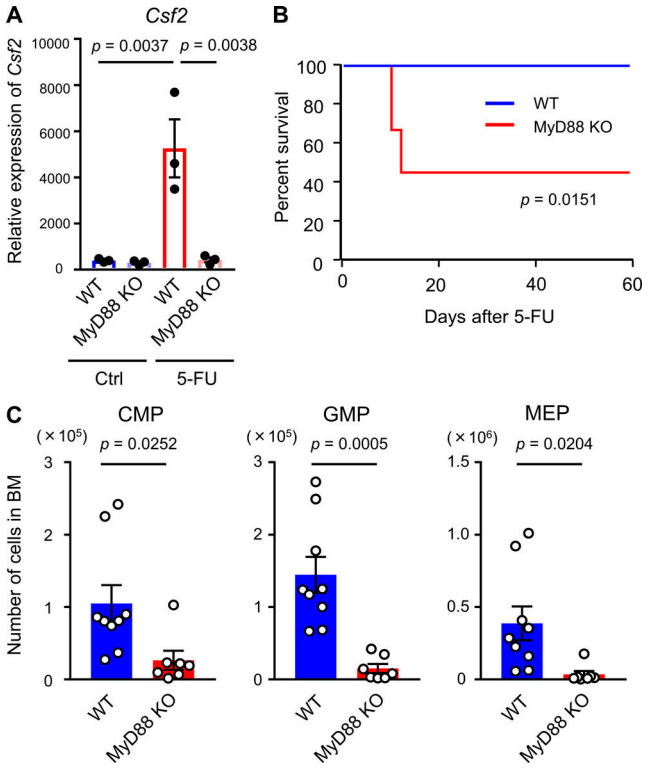

Figure 6. **MyD88 deficiency shows a phenocopy of GM-CSF deficiency upon stress by 5-FU. (A)** qRT-PCR analyses for the expression of *Csf2* in BM ILC2s from WT and MyD88-KO mice; *n* = 3, representative of two independent experiments. **(B)** Kaplan–Meier survival curves. WT (blue line) or MyD88-KO mice (red line) were treated with a single dose of 200 mg/kg 5-FU; *n* = 8 in WT, *n* = 9 in KO. Data are pooled from two independent experiments. **(C)** WT and MyD88-KO mice were treated with 150 mg/kg 5-FU, and BM cellularity was analyzed on day 8. The numbers of CMPs, GMPs, and MEPs from femurs and tibias are shown; *n* = 9 in WT, *n* = 7 in KO. Data are pooled from two independent experiments. In the bar charts, the results are shown as mean ± SEM, and each dot represents an individual mouse. Statistical significance was determined by ANOVA with the Bonferroni post hoc test (A), log-rank test (B), or unpaired Student's *t* test (C). Ctrl, control.

recovery after myeloablation by producing cytokines (Bowers et al., 2018; Olson et al., 2013; Zhao et al., 2014; Zhou et al., 2015). Although our current study also indicated that cross-talk among hematopoietic cells is needed for hematopoietic regeneration, we discovered that ILC2, expressing a high level of *Csf2*, is a key component for BM recovery.

GM-CSF is a powerful hematopoietic growth factor for myeloid differentiation from precursor cells, and also promotes cell survival, proliferation, and activation of macrophages (Hamilton, 2008). GM-CSF is synthesized by a variety of cells in response to inflammatory conditions or cytokines such as IL-1, IL-6, and TNF-α, whereas the production is restricted in the steady-state (Ushach and Zlotnik, 2016). GM-CSF promotes macrophages toward a proinflammatory phenotype, and numerous reports have shown that the blockade or depletion of GM-CSF results in significant suppression of autoimmune diseases (Hamilton, 2015). In addition, a recent report showed that synovial stromal cells and ILCs secreting GM-CSF initiate and augment arthritis in an autoimmune arthritis model (Hirota et al., 2018). The blockade of GM-CSF produced in pathological conditions has been the main target for controlling rheumatoid arthritis. In contrast, the administration of recombinant human CSFs (G-CSF and GM-CSF) has been used as a beneficial approach for patients with malignancy after chemotherapy or HSC transplantation, enhancing absolute neutrophil count recovery (Jones et al., 1996). GM-CSF–KO mice do not have a marked deficiency in hematopoiesis (Stanley et al., 1994), and our data also indicated that GM-CSF is not essential for BM hematopoiesis under homeostatic conditions. While we found that the signal from GM-CSF was activated in LSK cells, this molecule seems to be indispensable for myeloid differentiation during the process of BM recovery. Since the receptor of GM-CSF (*Csf2ra*) is expressed by not only HSPCs but also more committed hematopoietic cells in BM (Seita et al., 2012), GM-CSF after 5-FU treatment might target multiple stages of myeloid cells in BM. Importantly, GM-CSF could not be detected in PB before and after 5-FU, suggesting that GM-CSF functions locally in BM microenvironments. Our present data do not completely exclude the possibility that stromal or hematopoietic cells other than ILC2s contribute to GM-CSF production after BM stress. Nevertheless, our qRT-PCR and single-cell RNA-seq analyses of BM cells strongly support the conclusion that BM ILC2s are a critical population responsible for GM-CSF production.

There is increasing evidence to suggest that ILC2s are maintained locally and the ILC2s in BM do not replenish the pool of resident ILC2s in steady-state (Gasteiger et al., 2015; Moro et al., 2016), raising a question regarding the role of BM ILC2s. In this study, we show that BM ILC2s function locally similar to other tissue-resident ILC2s; they start to secrete large amounts of GM-CSF protein in response to BM damage, indicating that BM ILC2s are involved in tissue repair. We also scrutinized how GM-CSF secreted by ILC2s serves a protective function for tissue homeostasis. A recent report showed that IL-33 is expressed in B cell progenitors in the steady-state, whereas its deficiency does not impair B cell development (Stier et al., 2019). Dying B cell progenitors that are highly sensitive to 5-FU apparently support BM recovery through ILC2s, raising the possibility that there might be a B cell–ILC2 axis in BM injury. Since a previous report showed that the concentration of IL-33 in BM serum was increased after TBI and that the deficiency of IL-33 receptor (ST2) resulted in decreased mouse survival after TBI (Huang et al., 2019), ILC2s activated by IL-33 might also play a central role during BM recovery after TBI as seen in our 5-FU model. Importantly, a substantial number of ILC2s were alive after BM stress, indicating that ILC2s are predominantly preserved cells. Based on these findings, it is reasonable to speculate that BM ILC2s, among the various types of hematopoietic components, specifically play an essential role in myeloid recovery. While we demonstrated that transferred ILC2s derived from BM was homing to the BM cavity of 5-FU–treated mice, they might also migrate and contribute to tissue repair in other organs. We also found that MyD88 is an essential molecule for the up-regulation of *Csf2* in ILC2s. Since 5-FU–treated MyD88-KO mice showed a marked reduction in survival and serious suppression of myeloid recovery, MyD88 was supposed to be critical in the process of

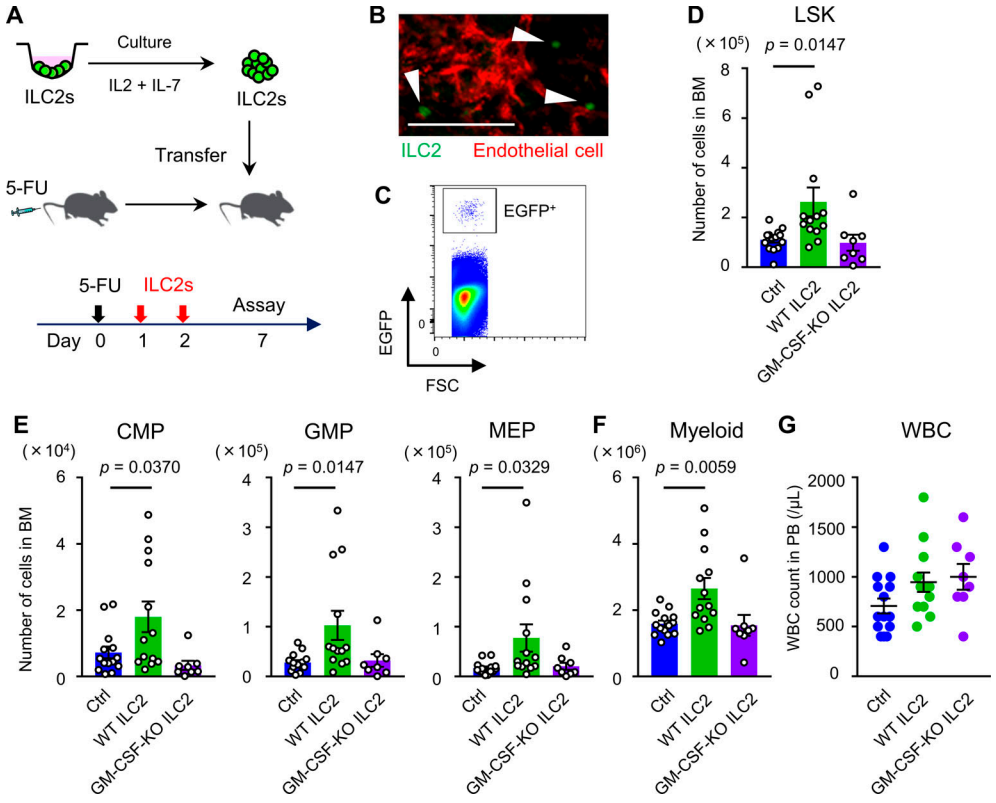

Figure 7. **BM ILC2s accelerate hematopoietic recovery after 5-FU treatment.** ILC2s from WT, CAG-EGFP, or GM-CSF–KO mice were sorted and cultured in medium supplemented with 10 ng/ml IL-2 and 10 ng/ml IL-7 to expand cell number. Then, 2 × 10^5 cells were intravenously injected into 150 mg/kg 5-FU–treated WT mice on days 1 and 2. **(A)** Schematic figure of the experiment. **(B and C)** WT mice were transferred with ILC2s from CAG-EGFP mice. On the day after the last transfer, the lodgment of EGFP⁺ cells in recipient BM was confirmed. **(B)** Snapshot of skull BM using two-photon microscopy. Green (arrowhead): EGFP⁺ ILC2; red: isolectin⁺ ECs. Scale bar, 100 µm. Results shown are representative of two independent experiments. **(C)** Flow cytometry plot of femur BM. Gated fraction represents homed EGFP⁺ ILC2s. Results shown are representative of two independent experiments. **(D–G)** WT mice were transferred with ILC2s from WT or GM-CSF–KO mice after 5-FU treatment. Control (Ctrl) mice were injected with PBS. The numbers of LSK (D), CMPs, GMPs, and MEPs (E), and Gr1⁺ or CD11b⁺ myeloid cells (F) from femurs and tibias, and WBC count in PB (G) were analyzed on day 7; n = 14 in control, n = 13 in WT ILC2s, and n = 8–10 in GM-CSF–KO ILC2s. Data are pooled from two independent experiments. In the bar charts, the results are shown as mean ± SEM, and each dot represents an individual mouse. Statistical significance was determined by ANOVA with the Bonferroni post hoc test (D–G).

myeloid recovery. MyD88 is an adaptor protein that propagates the response to both TLRs and IL-1 receptor family members. It is possible that TLR signaling is also activated in ILC2s after BM injury, as it was reported that in vitro stimulation of synovial ILCs with a TLR-9 ligand in combination with IL-33 increased GM-CSF production (Hirota et al., 2018). In addition, IL-1, a key emergency signal released by injured cells, might be involved in the activation of ILC2s. Further studies would resolve the role of the TLR signaling pathway during BM recovery.

Accumulating evidence has shown that the HSC niche is mainly composed of perivascular cells, including ECs and mesenchymal stromal cells (Morrison and Scadden, 2014). Our imaging data indicate that engrafted HSPCs locate around the vasculature and receive anti-apoptotic or proliferative signals there. Additionally, we found that signals from angiocrine factors, such as VEGF, were activated in HSPCs transplanted into 5-FU–treated mice. These results complement previous reports showing the importance of angiocrine factors for the regeneration of ECs and the reconstitution of HSPCs (Gaugler et al., 2001; Hooper et al., 2009; Kopp et al., 2005). Thus, regeneration of BM cells after a period of stress is performed mainly in perivascular areas. Nevertheless, whether activated ILC2s directly stimulate HSPCs in contact with them remains unknown since the spatial relationship between HSPCs and ILC2s in BM could not be analyzed due to technical difficulties. Further studies would resolve this question.

In summary, we address a fundamental question regarding the trigger of hematopoietic recovery at an early time point in BM injury. GM-CSF produced by ILC2s is crucial for BM recovery. While the administration of recombinant human G-CSF is generally used for absolute neutrophil count recovery, recombinant GM-CSF is not widely used due to a higher incidence of side effects compared with G-CSF. Nevertheless, our data raise the possibility that short-term and locally effective GM-CSF administration may play a key role in BM recovery. An improved understanding of how GM-CSF and other growth factors modulate the balance between self-renewal and differentiation of HSPCs in stressed microenvironment will provide clues for better adjunct therapy aimed at early hematopoietic recovery and for the development of ex vivo expansion of HSCs.

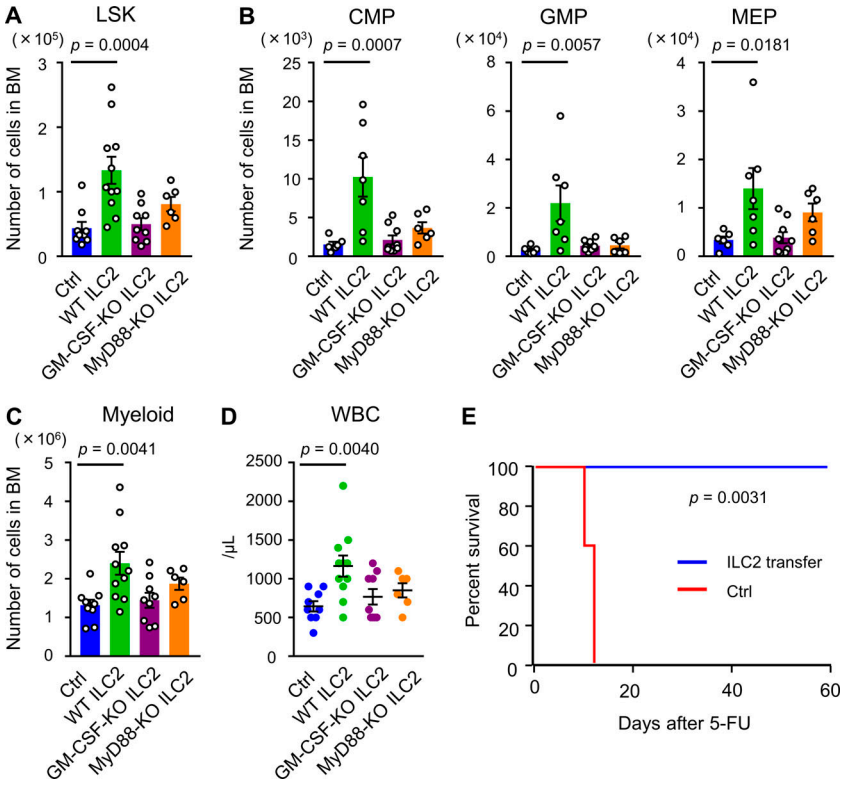

Figure 8. **BM ILC2s from WT mice rescue lethality of GM-CSF–KO mice by 5-FU. (A–D)** GM-CSF–KO mice were treated with 150 mg/kg 5-FU. Then, 2 × 10^5 ILC2s from WT, GM-CSF–KO, or MyD88-KO mice were intravenously injected on days 1 and 2. Control (Ctrl) mice were injected with PBS. The numbers of LSK (A), CMPs, GMPs, and MEPs (B), and Gr1$^+$ or CD11b$^+$ myeloid cells (C) from femurs and tibias, and WBC count in PB (D) were analyzed on day 7; n = 6–9 in control, n = 7–11 in WT ILC2s, n = 9 in GM-CSF–KO ILC2s, and n = 6 in MyD88-KO ILC2s. Data are pooled from two independent experiments. **(E)** Kaplan–Meier survival curves. GM-CSF–KO mice were treated with a single dose of 200 mg/kg 5-FU. In the ILC2 rescue group, mice were transferred with 2 × 10^5 ILC2s from WT mice on days 1 and 2 (blue line). Control mice were injected with PBS (red line); n = 5, representative of two independent experiments. In the bar charts, the results are shown as mean ± SEM, and each dot represents an individual mouse. Statistical significance was determined by ANOVA with the Bonferroni post hoc test (A–D) or the log-rank test (E).

Materials and methods

For additional information on materials used, see Table S3.

Mice

WT C57BL/6 mice were obtained from CLEA Japan. GM-CSF–KO (B6.129S-*Csf2*^{tm1Mlg}/J) mice (Dranoff et al., 1994) were obtained from The Jackson Laboratory. C57BL/6-Tg (CAG-EGFP) mice (Okabe et al., 1997) were obtained from Japan SLC. MyD88-KO (B6.129-Myd88^{tm1Aki}/Obs) mice (Adachi et al., 1998) were obtained from Oriental Bio Service. CXCL12-GFP mice were developed as previously reported (Sugiyama et al., 2006). IL-33$^{GFP/+}$ and IL-33$^{GFP/GFP}$ (IL-33–deficient) mice (Oboki et al., 2010) were kindly provided by S. Nakae (University of Tokyo, Tokyo, Japan) and H. Kiyonari (RIKEN, Kobe, Japan; accession no. CDB0631K; http://www.clst.riken.jp/arg/mutant%20mice%20list.html). These mouse lines were maintained on a C57BL/6 background. All mice used in this study were 8–14 wk old. Animal studies were performed with the approval of the Institutional Review Board of Osaka University.

Chemical and Ab treatment

Mice were treated with a single intravenous 200 mg/kg 5-FU (Kyowa-Hakko Kirin) injection to develop the BM stress model. Mice were sacrificed to perform expression assays (ELISA or qRT-PCR) or flow cytometry plots on day 0 (control) or day 2 (5-FU) after 5-FU treatment. To evaluate the recovery of BM cells after 5-FU treatment, WT, GM-CSF–KO, IL-33$^{GFP/GFP}$, or MyD88-KO mice were treated with a single intravenous dose of 150 mg/kg 5-FU and analyzed on day 8. To reduce ILC2s in BM, mice were injected with 200 μg anti-CD90.2 Ab (clone 30H12; Bio X Cell) intraperitoneally every other day four times until 1 d before 5-FU injection.

PB analyses after 5-FU treatment

PB samples were obtained by cardiac puncture. WBCs, hemoglobin, and platelet counts in PB were examined using a blood cell analyzer (KX-21; Sysmex).

Flow cytometry

BM cells were isolated by flushing the femurs and tibias. The marrow was flushed with staining buffer (PBS supplemented with 3% FBS, 4 mM EDTA, 100 U/ml penicillin, and 100 μg/ml streptomycin) by using a needle and syringe. Next, they were stained with the indicated Abs. Doublets were excluded by FSC and SSC profiles. Lineage (CD11b, Gr1, CD3ε, CD45R/B220, and Ter119)$^-$ Sca1$^+$ c-Kit^{Hi} (LSK) cells, CD48$^-$CD150$^+$ LSK cells, Lin$^-$c-Kit$^+$Sca1$^-$FCγR^{Lo}CD34$^+$ CMPs, Lin$^-$c-Kit$^+$Sca1$^-$FCγR^{Hi}CD34$^+$ GMPs, and Lin$^-$c-Kit$^+$Sca1$^-$FCγR^{Lo}CD34$^-$ MEPs were stained as previously described (Akashi et al., 2000; Kiel et al., 2005). To distinguish ILC2s from other differentiated cells, anti-lineage marker (CD3ε, CD4, CD8α, CD11c, FcεRIα, NK1.1, CD19, Ter119, CD5, F4/80, and Gr1) Abs were used (Moro et al., 2015). ILC2s were stained as Lin$^-$CD25$^+$IL-7Rα$^+$IL-33R$^+$ cells. B cell progenitors in BM, including pre-pro-B (B220$^+$IgM$^-$CD19$^-$CD43$^+$), pro-B (B220$^+$IgM$^-$CD19$^+$CD43$^+$), large pre-B (B220$^+$IgM$^-$CD19$^+$CD43$^-$FSC^{Hi}SSC^{Hi}), small pre-B (B220$^+$IgM$^-$CD19$^+$CD43$^-$FSC^{Lo}SSC^{Lo}), and immature B (B220^{Lo}IgM$^+$) cells, were stained as previously reported (Fukuhara et al., 2012; Stier et al., 2019). The numbers of cells in the femurs and tibias were obtained by multiplying the percentage of each population by total BM cells. To obtain BM samples, including ECs and stromal cells, bone samples were flushed with HBSS. Then, samples were incubated with 3 mg/ml collagenase type I (Worthington) and 100 μg/ml DNase I (Roche) for 30 min at 37°C. ECs were stained as Lin$^-$CD45$^-$Sca1$^+$CD31$^+$

cells. For staining of intracellular GM-CSF, BM cells were stimulated for 4–6 h in MEM α containing 10% FBS (Sigma-Aldrich), 50 ng/ml PMA (Sigma-Aldrich), 1 µg/ml ionomycin (Calbiochem), and GolgiStop (BD Biosciences) at the recommended concentration. The cells were stained with surface markers and were fixed and permeabilized with IntraPrep Permeabilization Reagent (Beckman Coulter). Then, cells were stained with anti–GM-CSF or isotype control Ab. To analyze BrdU uptake in vivo, mice were injected with 1 mg BrdU intraperitoneally 2 h before euthanization. BM cells were first stained with anti-Lin, c-Kit, and Sca1 Abs, then fixed and permeabilized using the BrdU Flow Kit (BD Biosciences). After treating cells with DNase to expose incorporated BrdU, cells were then stained with APC-conjugated anti-BrdU Ab (BD Biosciences) for 30 min at room temperature. Flow-cytometric analyses were performed with FACSCanto ll, FACSAria lll (BD Biosciences), or SH800 (Sony). Flow cytometry data were analyzed using FlowJo v.10 (FlowJo, LLC).

Cell isolation

For the sorting of HSPCs, BM cells were first incubated with biotinylated anti-Lin (CD11b, Gr1, CD3ε, CD45R/B220, and Ter119) Abs, followed by anti-biotin microbeads (Miltenyi Biotec). An AutoMACS separation column (Miltenyi Biotec) was used to remove Lin^+ cells. After Lin^--enriched cells were stained with anti-Lin, Sca1, and c-Kit Abs, LSK cells were sorted. B lymphocytes, T lymphocytes, monocytes, and neutrophils were sorted as $CD19^+$, $CD3ε^+$, $CD115^+$, and $CD11b^+Ly6G^+$ cells, respectively. For the sorting of ILC2s, BM cells were first incubated with biotinylated anti-Lin (CD3ε, CD4, CD8α, CD11c, FcεRIα, NK1.1, CD19, Ter119, CD5, F4/80, and Gr1) Abs, followed by anti-biotin microbeads. An AutoMACS separation column was used to remove Lin^+ cells. After Lin^--enriched cells were stained with anti-Lin, CD25, IL-7Rα, and IL-33R Abs, $Lin^-CD25^+IL\text{-}7Rα^+IL\text{-}33R^+$ ILC2s were sorted. Stromal cells, CAR cells, and ECs in BM were isolated after flushing the bone samples, followed by enzymatic incubation with collagenase type I and DNase I as mentioned before. CAR cells and stromal cells were isolated as $Sca1^-CD45^-Ter119^-CD31^-CXCL12\text{-}EGFP^{Hi}$ or $PDFGRβ^+Sca1^-CD31^-CD45^-Ter119^-$ fractions (Omatsu et al., 2014; Seike et al., 2018). ECs were isolated as $Lin^-CD45^-Sca1^+CD31^+$ cells (Schepers et al., 2012). Cells were sorted with an SH800 (Sony).

Intravital two-photon imaging of transplanted HSPCs

LSK cells were sorted from WT BM and stained with 10 µM of cell tracker CMFDA (Thermo Fisher Scientific) for 10 min. Cells ($1.5–2.4 \times 10^5$) were transplanted into nontreated control or 5-FU–treated WT mouse. 2 d before transplantation, 5-FU (200 mg/kg) was intravenously administered. After 24 h of transplantation, in vivo imaging of the skull BM was performed. The details of the imaging technique were described previously (Furuya et al., 2018). The frontoparietal regions of the skull bones were surgically exposed, and BM cavities were observed. After the number of HSPCs in the visualized whole skull bone area of each recipient was counted by eye under a mercury lamp, time-lapse imaging was performed. The imaging system consisted of a Nikon upright two-photon microscope (A1R-MP) equipped with a 25× water-immersion objective (APO, NA 1.1; Nikon). The system was laser-driven (Chameleon Vision II Ti: Sapphire; Coherent, Inc.), and the excitation wavelength was 840 nm in this study. Image stacks were collected at a depth of ∼150 µm (3 µm vertical steps) below the endosteal surface with 512 × 512 X-Y resolution, a time resolution of 2 min, and a duration of 2 h. ECs were stained by intravenous injection of 10 µg Alexa Fluor 594–conjugated isolectin GS-IB4 (Thermo Fisher Scientific). Detection of bone tissues was achieved by second harmonic generation. All surgical procedures were performed on mice subjected to isoflurane inhalation anesthesia. Analyses of image data were performed using Imaris software v.8.3.1 (Bitplane). Automatic three-dimensional object tracking with Imaris Spots was aided by manual corrections to retrieve cell spatial coordinates over time. Displacement (µm/h) was obtained by distance from beginning to end of track divided by imaging time (h). To compute the shortest distance from each HSPC to the surface of ECs, we used "distance transformation," an extension function equipped in Imaris. The maximum intensity projection (MIP) images of the tiled z-stack and time-lapse videos from MIP images were made using NIS-Elements v.4.50.00 and Adobe After Effects CS6, respectively.

Intravital two-photon imaging of transferred ILC2s

ILC2s from CAG-EGFP mice were sorted and cultured to expand the number of cells. Then, 2×10^5 cells were injected intravenously into 150 mg/kg 5-FU–treated WT mice on days 1 and 2. On day 3, in vivo imaging of the skull BM was performed. ECs were stained by intravenous injection of Alexa Fluor 594–conjugated isolectin GS-IB4.

RNA-seq analyses of transplanted HSPCs

LSK cells in femurs and tibias were sorted from CAG-EGFP mice. Sorted cells (10^5 each) were transplanted into nontreated control or 5-FU–treated WT mice ($n = 2$). 2 d before transplantation, 200 mg/kg 5-FU was intravenously administered. 24 h after transplantation, BMMNCs from femurs and tibias of each recipient were collected using Lymphoprep (Axis-Shield). Then, $EGFP^+$ cells in the BM of each recipient mouse were resorted. RNA was purified using the miRNeasy Mini Kit (Qiagen) and amplified using the SMARTer Ultra Low RNA Kit (Clontech Laboratories) for preparing cDNA libraries. Sequencing was performed on an Illumina HiSeq 2500 platform (Illumina) in a 75-base single-end mode. Illumina Casava software (v1.8.2; Illumina) was used for base calling. Sequenced reads were mapped to mouse reference genome sequences (mm10) using TopHat (v2.0.13; https://ccb.jhu.edu/software/tophat/index.shtml) in combination with Bowtie2 (v2.2.3; http://bowtie-bio.sourceforge.net/bowtie2/index.shtml) and SAMtools (v0.1.19; http://samtools.sourceforge.net/). The fragments per kilobase of exon per million mapped fragments were calculated using Cufflinks (v2.2.1; http://cole-trapnell-lab.github.io/cufflinks/). Two criteria were used to normalize and compare the values of HSPCs (5-FU versus control) and define the signal ratios: more than a twofold increase or less than a twofold decrease. Bioinformatic analyses were conducted with Ingenuity Pathway Analysis

software (Ingenuity Systems; Qiagen). The heat map enables the visualization of the differential expression data of genes categorized by their functions using the Ingenuity Knowledge Base. The color bar indicates the z-score for each category: orange and blue squares correspond to strong predicted increase (z-score > 2) and decrease (z-score < −2), respectively. Gray and white indicate categories with a −2 < z-score < 2 and without z-score, respectively. Larger squares indicate a significantly higher overlap among the altered genes in the dataset. Upstream Regulator Analysis was performed to predict the activation or inhibition of transcriptional factors and growth factors based on the observed gene expression changes in the gene datasets. Statistical analysis of the predictions was calculated by the activation z-score, which is designed to ensure that gene sets composed of perturbed genes chosen randomly with random sign of fold change do not produce significant results on average. The strongest predicted activation corresponds to z-scores ≥ 2, and the strongest predicted inhibition corresponds to z-scores ≤ −2. Raw reads from these samples have been submitted to the Gene Expression Omnibus database of the National Center for Biotechnology Information (under accession no. GSE120113).

qRT-PCR analyses

RNA samples from LSK cells were isolated using the RNeasy Mini Kit (>5 × 10^5 cells) or Micro Kit (<5 × 10^5 cells; Qiagen). RT reactions were performed using the High-Capacity RNA-to-cDNA Kit (Applied Biosystems). Taqman FAM dye-labeled minor groove binder probe sets for *Gapdh* (Mm99999915), colony-stimulating factor 2 (*Csf2*; Mm01290062), vascular endothelial growth factor (*Vegfa*; Mm00437306), hepatocyte growth factor (*Hgf*; Mm01135184), angiopoietin-2 (*Angpt2*; Mm00545822), CSF2 receptor α subunit (*Csf2ra*; Mm00438331), CSF2 receptor β common subunit (*Csf2rb*; Mm00655745), and interleukin-33 (*Il33*; Mm00505403) were purchased from Applied Biosystems. The expression level of each gene was evaluated according to the Taqman Gene Expression Assay Protocol. Reactions were run on the 7900HT Fast Real-Time PCR system, and the data were analyzed using SDS v.2.4 software (Applied Biosystems). Data were normalized to the expression of *Gapdh*.

Single-cell RNA-seq analyses

BMMNCs from 5-FU (200 mg/kg) day 2 mice were prepared using Lymphoprep. Then, $Sca1^+$ cells were sorted, and targeted single-cell RNA-seq analysis was conducted using the BD Rhapsody Single-Cell Analysis System (BD Biosciences; Fan et al., 2015). In short, the single-cell suspension was loaded into a BD Rhapsody cartridge with >200,000 microwells, and single-cell capture was achieved by random distribution and gravity precipitation. Next, the bead library was loaded into the microwell cartridge to saturation so that a bead was paired with a cell in a microwell. The cells were lysed in the microwell cartridge to hybridize mRNA molecules onto bar-coded capture oligos on the beads. Then, these beads were retrieved from the microwell cartridge into a single tube for the subsequent steps of cDNA synthesis, exonuclease I digestion, and multiplex-PCR–based library construction. For the library construction, we used the BD Rhapsody Immune Response Panel for mouse (BD Biosciences) consisting of primer sets for 397 genes. Sequencing was performed on an Illumina HiSeq 3000 platform (100 × 2 bp). The BD Rhapsody Analysis Pipeline was used to process the sequencing data (fastq files), and output result files were analyzed and visualized by the BD Data View software v.1.2.2 (BD Biosciences). Hierarchical clustering on t-SNE analysis of 4,424 cells generated clusters. Then, highly expressed genes specific for each cluster were identified. To reveal the cell type of *Csf2*-expressing cells, correlated gene lists with correlation coefficient and P value were determined using BD Data View software. Raw reads from the sample have been submitted to the Gene Expression Omnibus database of the National Center for Biotechnology Information (accession no. GSE120113).

ELISA

To analyze GM-CSF protein levels in the BM, one femur of each mouse was flushed with 0.3 ml PBS containing 1% protease inhibitor cocktail (Sigma-Aldrich) and Nonidet P-40 (Nacalai Tesque). Cells were lysed by freeze and thaw, and the cell debris was removed by centrifugation. To analyze IL-33 protein levels in the BM, one femur of each mouse was flushed with 0.3 ml PBS, and the cell pellets were removed by centrifugation. GM-CSF and IL-33 were measured using the mGM-CSF ELISA Kit (Origene) and mouse/rat IL-33 Quantikine ELISA Kit (R&D Systems), according to the manufacturer's instructions. For the preparation of supernatants from 5-FU–treated B cells, $CD19^+$ cells that were enriched, using a magnetic column, from BM of WT mice were seeded at 1 × 10^6 cells per well into 48-well tissue culture plates in the presence of 10 mg/ml 5-FU as previously reported (Fang et al., 2014). Supernatants were collected after 24 h and were concentrated using the Vivaspin 500-10K (GE Healthcare). IL-33 levels were then measured using the mouse/rat IL-33 Quantikine ELISA Kit (R&D Systems).

Immunohistochemical analysis

WT mice at 5-FU day 2 (200 mg/kg) were intravenously injected with 7.5 µg Alexa Fluor 647–conjugated anti-mouse CD31 and CD144 Abs in 200 µl PBS to stain ECs in vivo. 15 min after injection, mice were anesthetized with isoflurane, and femoral bones were collected after perfusion-fixation with 4% (vol/vol) paraformaldehyde (PFA; Sigma-Aldrich). Dissected bone samples were further fixed in 4% PFA for 4 h and equilibrated in 30% sucrose/PBS. Fixed samples were embedded in Super Cryoembedding Medium (Section-LAB) and frozen in cooled hexane. Sections of undecalcified femoral bone were generated via Kawamoto's film method using Cryofilm (Section-LAB). The 7-µm-thick cryostat sections were first blocked/permeabilized in PBS containing 5% fetal calf serum, 55 µg/ml rabbit γ-globulin (Jackson ImmunoResearch), and 0.3% Triton X-100 (Sigma-Aldrich) for 30 min. Samples were stained with 5 µg/ml goat anti-mouse IL-33 Ab (R&D Systems) for 60 min, followed by incubation with 5 µg/ml Cy3-conjugated donkey anti-goat Ab (Jackson ImmunoResearch) for 30 min. Then, the same samples were stained with biotinylated rat anti-mouse CD19 Ab (BD Biosciences) for 60 min, followed by incubation with 5 µg/ml streptavidin–Alexa Fluor 488 (Thermo Fisher Scientific) for

30 min. The samples were washed two times, for 5 min each, after each Ab incubation. The sections were mounted with Vectashield mounting medium with DAPI (Vector) and imaged with a confocal microscope (A1R+; Nikon) using a laser at four different wavelengths (405, 488, 561, and 640 nm). Image analyses were performed using NIS-Element (Nikon).

In vitro culture and transfer of ILC2

BM ILC2s sorted from WT, GM-CSF–KO, MyD88-KO, or CAG-EGFP mice were seeded at 0.5–1 × 10^4 cells/well into round-bottomed 96-well plates in 10% FBS RPMI-1640 (Nacalai Tesque) complete medium containing 100 U/ml penicillin and 100 µg/ml streptomycin (Sigma-Aldrich), 50 µM 2-mercaptoethanol (Gibco), 2 mM L-glutamine (Gibco), 10 mM Hepes (Gibco), 1 mM sodium pyruvate (Gibco), 1 mM MEM nonessential amino acids solution (Gibco), 10 ng/ml IL-2 (R&D Systems), and 10 ng/ml IL-7 (R&D Systems) for 2–4 wk to expand the number of cells. Half of the culture medium was exchanged every 2 d. After expansion, 2 × 10^5 cells or PBS (control) was injected intravenously into recipient mice on days 1 and 2 after 5-FU treatment. The numbers of LSK cells, CMPs, GMPs, MEPs, and Gr1$^+$ or CD11b$^+$ myeloid cells from femurs and tibias, and WBC count in PB, were analyzed on day 7.

Whole-mount confocal imaging of femoral bones from CXCL12-GFP mice

CXCL12-GFP mice were treated with 150 mg/kg 5-FU, and 2 × 10^5 cultured ILC2s from WT mice or PBS (control) were intravenously injected on days 1 and 2. Then, whole-mount confocal imaging analysis of femoral bones was performed on day 7. Whole-mount tissue preparation was performed as previously reported (Kunisaki et al., 2013). Briefly, mice were anesthetized with isoflurane, and femoral bones were collected after perfusion-fixation with 4% (vol/vol) PFA. Dissected bone samples were further fixed in 4% PFA for 30 min and embedded in Super Cryoembedding Medium. Samples were shaved on a cryostat until the BM cavity was fully exposed. Then, samples were washed with PBS, set on glass-bottom dishes, mounted with Vectashield mounting medium (Vector), and imaged with a confocal microscope (A1R+; Nikon). The whole-mount bone images were collected with 3-µm vertical steps. Image analysis was performed using NIS-Element (Nikon). The CXCL12-GFP$^+$ areas, from the MIP images of the tiled z-stack, were binarized using Otsu's thresholding method. Then, the binary area fraction relative to the whole visual field was automatically calculated.

Statistical analysis

Data are presented as mean ± SEM unless otherwise stated. Experiments with two groups were analyzed with standard Student's *t* tests. The log-rank test was used to analyze survival data. Statistical significance was judged using ANOVA with the Bonferroni post hoc test for multiple comparisons. Statistical analyses were performed using Graphpad Prism v.7 software (GraphPad Software).

Online supplemental material

Fig. S1 shows the analyses of intravital two-photon microscopic imaging of BM. Fig. S2 shows bioinformatic analyses of HSPCs homed into 5-FU–treated BM. Fig. S3 shows the phenotype of GM-CSF–KO mice. Fig. S4 shows additional analyses of BM cells from WT, IL-33–GFP, and IL-33–deficient mice. Fig. S5 shows additional data from ILC2-depleted or ILC2-transferred mice. Video 1 shows in vivo imaging of skull BM of a steady-state mouse transplanted with HSPCs. Video 2 shows in vivo imaging of skull BM of a 5-FU–treated mouse transplanted with HSPCs. Table S1 lists highly expressed genes in ILC2 cluster cells. Table S2 lists genes that are highly coexpressed with *Csf2*. Table S3 lists Abs used in this study.

Acknowledgments

We thank Dr. S. Nakae (University of Tokyo, Tokyo, Japan) and Dr. H. Kiyonari (RIKEN, Kobe, Japan) for providing IL-33 mutant mice; Dr. R. Sugimura (University of Hong Kong) for guidance; Mr. K. Kubota (RIKEN), Dr. Y. Omatsu (Osaka University), Dr. Y. Kunisaki (Kyushu University), and Ms. M. Yorioka (Osaka University) for technical support; and Mr. N. Hosono and S. Matsumoto (BioStream) for their support in RNA-seq and data analysis.

This work was supported by CREST, Japan Science and Technology Agency (JPMJCR15G1 to M. Ishii); from the Japan Society for the Promotion of Science, a Grant-in-Aid for Scientific Research (S) (19H056570 to M. Ishii), a Grant-in-Aid for Research Activity start-up (15H06373 to T. Sudo), and Grants-in-Aid for Young Scientists (18K16114 and 20K17378 to T. Sudo); and grants from the Takeda Science Foundation (to M. Ishii and T. Sudo), the Osaka Cancer Society (to T. Sudo), and the Japanese Society of Hematology (to T. Sudo).

Author contributions: T. Sudo and M. Ishii designed the experiments and analyzed the data; T. Sudo, H. Mizuno, D. Okuzaki, Y. Motomura, J. Kikuta, T. Matsui, T. Hasegawa, D. Motooka, T. Ao, and R. Yoshizawa conducted the experiments; T. Sudo, D. Okuzaki, and M. Ishii wrote the manuscript; T. Yokota, K. Moro, Y. Kanakura, and T. Nagasawa provided scientific advice and materials; and M. Ishii conceived the project and supervised the research.

Disclosures: The authors declare no competing interests exist.

Submitted: 27 April 2020
Revised: 29 October 2020
Accepted: 2 February 2021

References

Adachi, O., T. Kawai, K. Takeda, M. Matsumoto, H. Tsutsui, M. Sakagami, K. Nakanishi, and S. Akira. 1998. Targeted disruption of the MyD88 gene results in loss of IL-1- and IL-18-mediated function. *Immunity.* 9: 143–150. https://doi.org/10.1016/S1074-7613(00)80596-8

Akashi, K., D. Traver, T. Miyamoto, and I.L. Weissman. 2000. A clonogenic common myeloid progenitor that gives rise to all myeloid lineages. *Nature.* 404:193–197. https://doi.org/10.1038/35004599

Bagby, G.C. Jr., C.A. Dinarello, P. Wallace, C. Wagner, S. Hefeneider, and E. McCall. 1986. Interleukin 1 stimulates granulocyte macrophage colony-stimulating activity release by vascular endothelial cells. *J. Clin. Invest.* 78:1316–1323. https://doi.org/10.1172/JCI112717

Bartemes, K.R., K. Iijima, T. Kobayashi, G.M. Kephart, A.N. McKenzie, and H. Kita. 2012. IL-33-responsive lineage- CD25+ CD44(hi) lymphoid cells

mediate innate type 2 immunity and allergic inflammation in the lungs. *J. Immunol.* 188:1503–1513. https://doi.org/10.4049/jimmunol.1102832

Bowers, E., A. Slaughter, P.S. Frenette, R. Kuick, O.M. Pello, and D. Lucas. 2018. Granulocyte-derived TNFα promotes vascular and hematopoietic regeneration in the bone marrow. *Nat. Med.* 24:95–102. https://doi.org/10.1038/nm.4448

Brickshawana, A., V.S. Shapiro, H. Kita, and L.R. Pease. 2011. Lineage(-) Scal+c-Kit(-)CD25+ cells are IL-33-responsive type 2 innate cells in the mouse bone marrow. *J. Immunol.* 187:5795–5804. https://doi.org/10.4049/jimmunol.1102242

Busch, K., K. Klapproth, M. Barile, M. Flossdorf, T. Holland-Letz, S.M. Schlenner, M. Reth, T. Höfer, and H.R. Rodewald. 2015. Fundamental properties of unperturbed haematopoiesis from stem cells in vivo. *Nature.* 518:542–546. https://doi.org/10.1038/nature14242

Decker, M., J. Leslie, Q. Liu, and L. Ding. 2018. Hepatic thrombopoietin is required for bone marrow hematopoietic stem cell maintenance. *Science.* 360:106–110. https://doi.org/10.1126/science.aap8861

Dinarello, C.A. 2018. Overview of the IL-1 family in innate inflammation and acquired immunity. *Immunol. Rev.* 281:8–27. https://doi.org/10.1111/imr.12621

Ding, L., T.L. Saunders, G. Enikolopov, and S.J. Morrison. 2012. Endothelial and perivascular cells maintain haematopoietic stem cells. *Nature.* 481:457–462. https://doi.org/10.1038/nature10783

Dranoff, G., A.D. Crawford, M. Sadelain, B. Ream, A. Rashid, R.T. Bronson, G.R. Dickersin, C.J. Bachurski, E.L. Mark, J.A. Whitsett, et al. 1994. Involvement of granulocyte-macrophage colony-stimulating factor in pulmonary homeostasis. *Science.* 264:713–716. https://doi.org/10.1126/science.8171324

Fan, H.C., G.K. Fu, and S.P. Fodor. 2015. Expression profiling. Combinatorial labeling of single cells for gene expression cytometry. *Science.* 347:1258367. https://doi.org/10.1126/science.1258367

Fang, H., B. Ang, X. Xu, X. Huang, Y. Wu, Y. Sun, W. Wang, N. Li, X. Cao, and T. Wan. 2014. TLR4 is essential for dendritic cell activation and anti-tumor T-cell response enhancement by DAMPs released from chemically stressed cancer cells. *Cell. Mol. Immunol.* 11:150–159. https://doi.org/10.1038/cmi.2013.59

Fraile, R.J., L.H. Baker, T.R. Buroker, J. Horwitz, and V.K. Vaitkevicius. 1980. Pharmacokinetics of 5-fluorouracil administered orally, by rapid intravenous and by slow infusion. *Cancer Res.* 40:2223–2228.

Fukuhara, S., S. Simmons, S. Kawamura, A. Inoue, Y. Orba, T. Tokudome, Y. Sunden, Y. Arai, K. Moriwaki, J. Ishida, et al. 2012. The sphingosine-1-phosphate transporter Spns2 expressed on endothelial cells regulates lymphocyte trafficking in mice. *J. Clin. Invest.* 122:1416–1426. https://doi.org/10.1172/JCI60746

Furuya, M., J. Kikuta, S. Fujimori, S. Seno, H. Maeda, M. Shirazaki, M. Uenaka, H. Mizuno, Y. Iwamoto, A. Morimoto, et al. 2018. Direct cell-cell contact between mature osteoblasts and osteoclasts dynamically controls their functions in vivo. *Nat. Commun.* 9:300. https://doi.org/10.1038/s41467-017-02541-w

Gasteiger, G., X. Fan, S. Dikiy, S.Y. Lee, and A.Y. Rudensky. 2015. Tissue residency of innate lymphoid cells in lymphoid and nonlymphoid organs. *Science.* 350:981–985. https://doi.org/10.1126/science.aac9593

Gaugler, M.H., C. Squiban, M.A. Mouthon, P. Gourmelon, and A. van der Meeren. 2001. Irradiation enhances the support of haemopoietic cell transmigration, proliferation and differentiation by endothelial cells. *Br. J. Haematol.* 113:940–950. https://doi.org/10.1046/j.1365-2141.2001.02852.x

Hamilton, J.A. 2008. Colony-stimulating factors in inflammation and autoimmunity. *Nat. Rev. Immunol.* 8:533–544. https://doi.org/10.1038/nri2356

Hamilton, J.A. 2015. GM-CSF as a target in inflammatory/autoimmune disease: current evidence and future therapeutic potential. *Expert Rev. Clin. Immunol.* 11:457–465. https://doi.org/10.1586/1744666X.2015.1024110

Heissig, B., K. Hattori, S. Dias, M. Friedrich, B. Ferris, N.R. Hackett, R.G. Crystal, P. Besmer, D. Lyden, M.A. Moore, et al. 2002. Recruitment of stem and progenitor cells from the bone marrow niche requires MMP-9 mediated release of kit-ligand. *Cell.* 109:625–637. https://doi.org/10.1016/S0092-8674(02)00754-7

Hérault, A., M. Binnewies, S. Leong, F.J. Calero-Nieto, S.Y. Zhang, Y.A. Kang, X. Wang, E.M. Pietras, S.H. Chu, K. Barry-Holson, et al. 2017. Myeloid progenitor cluster formation drives emergency and leukaemic myelopoiesis. *Nature.* 544:53–58. https://doi.org/10.1038/nature21693

Hirota, K., M. Hashimoto, Y. Ito, M. Matsuura, H. Ito, M. Tanaka, H. Watanabe, G. Kondoh, A. Tanaka, K. Yasuda, et al. 2018. Autoimmune Th17 Cells Induced Synovial Stromal and Innate Lymphoid Cell Secretion of the Cytokine GM-CSF to Initiate and Augment Autoimmune Arthritis. *Immunity.* 48:1220–1232.e5. https://doi.org/10.1016/j.immuni.2018.04.009

Hooper, A.T., J.M. Butler, D.J. Nolan, A. Kranz, K. Iida, M. Kobayashi, H.G. Kopp, K. Shido, I. Petit, K. Yanger, et al. 2009. Engraftment and reconstitution of hematopoiesis is dependent on VEGFR2-mediated regeneration of sinusoidal endothelial cells. *Cell Stem Cell.* 4:263–274. https://doi.org/10.1016/j.stem.2009.01.006

Hoyler, T., C.S. Klose, A. Souabni, A. Turqueti-Neves, D. Pfeifer, E.L. Rawlins, D. Voehringer, M. Busslinger, and A. Diefenbach. 2012. The transcription factor GATA-3 controls cell fate and maintenance of type 2 innate lymphoid cells. *Immunity.* 37:634–648. https://doi.org/10.1016/j.immuni.2012.06.020

Huang, P., X. Li, Y. Meng, B. Yuan, T. Liu, M. Jiao, X. Wang, Y. Liu, and H. Yin. 2019. Interleukin-33 regulates hematopoietic stem cell regeneration after radiation injury. *Stem Cell Res. Ther.* 10:123. https://doi.org/10.1186/s13287-019-1221-1

Hui, C.C., K.M. McNagny, J.A. Denburg, and M.C. Siracusa. 2015. In situ hematopoiesis: a regulator of TH2 cytokine-mediated immunity and inflammation at mucosal surfaces. *Mucosal Immunol.* 8:701–711. https://doi.org/10.1038/mi.2015.17

Inclan-Rico, J.M., C.M. Hernandez, E.K. Henry, H.G. Federman, C.B. Sy, J.J. Ponessa, A.D. Lemenze, N. Joseph, P. Soteropoulos, A.M. Beaulieu, et al. 2020. Trichinella spiralis-induced mastocytosis and erythropoiesis are simultaneously supported by a bipotent mast cell/erythrocyte precursor cell. *PLoS Pathog.* 16:e1008579. https://doi.org/10.1371/journal.ppat.1008579

Jones, S.E., M.W. Schottstaedt, L.A. Duncan, R.L. Kirby, R.H. Good, R.G. Mennel, T.K. George, D.A. Snyder, D.L. Watkins, C.A. Denham, et al. 1996. Randomized double-blind prospective trial to evaluate the effects of sargramostim versus placebo in a moderate-dose fluorouracil, doxorubicin, and cyclophosphamide adjuvant chemotherapy program for stage II and III breast cancer. *J. Clin. Oncol.* 14:2976–2983. https://doi.org/10.1200/JCO.1996.14.11.2976

Karigane, D., H. Kobayashi, T. Morikawa, Y. Ootomo, M. Sakai, G. Nagamatsu, Y. Kubota, N. Goda, M. Matsumoto, E.K. Nishimura, et al. 2016. p38α Activates Purine Metabolism to Initiate Hematopoietic Stem/Progenitor Cell Cycling in Response to Stress. *Cell Stem Cell.* 19:192–204. https://doi.org/10.1016/j.stem.2016.05.013

Kiel, M.J., O.H. Yilmaz, T. Iwashita, O.H. Yilmaz, C. Terhorst, and S.J. Morrison. 2005. SLAM family receptors distinguish hematopoietic stem and progenitor cells and reveal endothelial niches for stem cells. *Cell.* 121:1109–1121. https://doi.org/10.1016/j.cell.2005.05.026

Koga, S., K. Hozumi, K.I. Hirano, M. Yazawa, T. Terooatea, A. Minoda, T. Nagasawa, S. Koyasu, and K. Moro. 2018. Peripheral PDGFRα^{+}gp38^{+} mesenchymal cells support the differentiation of fetal liver-derived ILC2. *J. Exp. Med.* 215:1609–1626. https://doi.org/10.1084/jem.20172310

Kopp, H.-G., S.T. Avecilla, A.T. Hooper, S.V. Shmelkov, C.A. Ramos, F. Zhang, and S. Rafii. 2005. Tie2 activation contributes to hemangiogenic regeneration after myelosuppression. *Blood.* 106:505–513. https://doi.org/10.1182/blood-2004-11-4269

Kunisaki, Y., I. Bruns, C. Scheiermann, J. Ahmed, S. Pinho, D. Zhang, T. Mizoguchi, Q. Wei, D. Lucas, K. Ito, et al. 2013. Arteriolar niches maintain haematopoietic stem cell quiescence. *Nature.* 502:637–643. https://doi.org/10.1038/nature12612

Li, B.W.S., R. Stadhouders, M.J.W. de Bruijn, M. Lukkes, D.M.J.M. Beerens, M.D. Brem, A. KleinJan, I. Bergen, H. Vroman, M. Kool, et al. 2017. Group 2 Innate Lymphoid Cells Exhibit a Dynamic Phenotype in Allergic Airway Inflammation. *Front. Immunol.* 8:1684. https://doi.org/10.3389/fimmu.2017.01684

Lo Celso, C., H.E. Fleming, J.W. Wu, C.X. Zhao, S. Miake-Lye, J. Fujisaki, D. Côté, D.W. Rowe, C.P. Lin, and D.T. Scadden. 2009. Live-animal tracking of individual haematopoietic stem/progenitor cells in their niche. *Nature.* 457:92–96. https://doi.org/10.1038/nature07434

Lukens, J.R., M.J. Barr, D.D. Chaplin, H. Chi, and T.D. Kanneganti. 2012. Inflammasome-derived IL-1β regulates the production of GM-CSF by CD4(+) T cells and γδ T cells. *J. Immunol.* 188:3107–3115. https://doi.org/10.4049/jimmunol.1103308

Lüthi, A.U., S.P. Cullen, E.A. McNeela, P.J. Duriez, I.S. Afonina, C. Sheridan, G. Brumatti, R.C. Taylor, K. Kersse, P. Vandenabeele, et al. 2009. Suppression of interleukin-33 bioactivity through proteolysis by apoptotic caspases. *Immunity.* 31:84–98. https://doi.org/10.1016/j.immuni.2009.05.007

Min, L., S.A. Isa, W.N. Fam, S.K. Sze, O. Beretta, A. Mortellaro, and C. Ruedl. 2012. Synergism between curdlan and GM-CSF confers a strong

inflammatory signature to dendritic cells. *J. Immunol.* 188:1789–1798. https://doi.org/10.4049/jimmunol.1101755

Monticelli, L.A., L.C. Osborne, M. Noti, S.V. Tran, D.M. Zaiss, and D. Artis. 2015. IL-33 promotes an innate immune pathway of intestinal tissue protection dependent on amphiregulin-EGFR interactions. *Proc. Natl. Acad. Sci. USA.* 112:10762–10767. https://doi.org/10.1073/pnas.1509070112

Moro, K., T. Yamada, M. Tanabe, T. Takeuchi, T. Ikawa, H. Kawamoto, J. Furusawa, M. Ohtani, H. Fujii, and S. Koyasu. 2010. Innate production of T(H)2 cytokines by adipose tissue-associated c-Kit(+)Sca-1(+) lymphoid cells. *Nature.* 463:540–544. https://doi.org/10.1038/nature08636

Moro, K., K.N. Ealey, H. Kabata, and S. Koyasu. 2015. Isolation and analysis of group 2 innate lymphoid cells in mice. *Nat. Protoc.* 10:792–806. https://doi.org/10.1038/nprot.2015.047

Moro, K., H. Kabata, M. Tanabe, S. Koga, N. Takeno, M. Mochizuki, K. Fukunaga, K. Asano, T. Betsuyaku, and S. Koyasu. 2016. Interferon and IL-27 antagonize the function of group 2 innate lymphoid cells and type 2 innate immune responses. *Nat. Immunol.* 17:76–86. https://doi.org/10.1038/ni.3309

Morrison, S.J., and D.T. Scadden. 2014. The bone marrow niche for haematopoietic stem cells. *Nature.* 505:327–334. https://doi.org/10.1038/nature12984

Moussion, C., N. Ortega, and J.P. Girard. 2008. The IL-1-like cytokine IL-33 is constitutively expressed in the nucleus of endothelial cells and epithelial cells in vivo: a novel 'alarmin'? *PLoS One.* 3:e3331. https://doi.org/10.1371/journal.pone.0003331

Neill, D.R., S.H. Wong, A. Bellosi, R.J. Flynn, M. Daly, T.K. Langford, C. Bucks, C.M. Kane, P.G. Fallon, R. Pannell, et al. 2010. Nuocytes represent a new innate effector leukocyte that mediates type-2 immunity. *Nature.* 464:1367–1370. https://doi.org/10.1038/nature08900

Oboki, K., T. Ohno, N. Kajiwara, K. Arae, H. Morita, A. Ishii, A. Nambu, T. Abe, H. Kiyonari, K. Matsumoto, et al. 2010. IL-33 is a crucial amplifier of innate rather than acquired immunity. *Proc. Natl. Acad. Sci. USA.* 107:18581–18586. https://doi.org/10.1073/pnas.1003059107

Okabe, M., M. Ikawa, K. Kominami, T. Nakanishi, and Y. Nishimune. 1997. 'Green mice' as a source of ubiquitous green cells. *FEBS Lett.* 407:313–319. https://doi.org/10.1016/S0014-5793(97)00313-X

Olson, T.S., A. Caselli, S. Otsuru, T.J. Hofmann, R. Williams, P. Paolucci, M. Dominici, and E.M. Horwitz. 2013. Megakaryocytes promote murine osteoblastic HSC niche expansion and stem cell engraftment after radioablative conditioning. *Blood.* 121:5238–5249. https://doi.org/10.1182/blood-2012-10-463414

Omatsu, Y., M. Seike, T. Sugiyama, T. Kume, and T. Nagasawa. 2014. Foxc1 is a critical regulator of haematopoietic stem/progenitor cell niche formation. *Nature.* 508:536–540. https://doi.org/10.1038/nature13071

Pietras, E.M., C. Mirantes-Barbeito, S. Fong, D. Loeffler, L.V. Kovtonyuk, S. Zhang, R. Lakshminarasimhan, C.P. Chin, J.M. Techner, B. Will, et al. 2016. Chronic interleukin-1 exposure drives haematopoietic stem cells towards precocious myeloid differentiation at the expense of self-renewal. *Nat. Cell Biol.* 18:607–618. https://doi.org/10.1038/ncb3346

Qian, H., N. Buza-Vidas, C.D. Hyland, C.T. Jensen, J. Antonchuk, R. Månsson, L.A. Thoren, M. Ekblom, W.S. Alexander, and S.E. Jacobsen. 2007. Critical role of thrombopoietin in maintaining adult quiescent hematopoietic stem cells. *Cell Stem Cell.* 1:671–684. https://doi.org/10.1016/j.stem.2007.10.008

Rana, B.M.J., E. Jou, J.L. Barlow, N. Rodriguez-Rodriguez, J.A. Walker, C. Knox, H.E. Jolin, C.S. Hardman, M. Sivasubramaniam, A. Szeto, et al. 2019. A stromal cell niche sustains ILC2-mediated type-2 conditioning in adipose tissue. *J. Exp. Med.* 216:1999–2009. https://doi.org/10.1084/jem.20190689

Randall, T.D., and I.L. Weissman. 1997. Phenotypic and functional changes induced at the clonal level in hematopoietic stem cells after 5-fluorouracil treatment. *Blood.* 89:3596–3606. https://doi.org/10.1182/blood.V89.10.3596

Schepers, K., E.C. Hsiao, T. Garg, M.J. Scott, and E. Passegué. 2012. Activated Gs signaling in osteoblastic cells alters the hematopoietic stem cell niche in mice. *Blood.* 120:3425–3435. https://doi.org/10.1182/blood-2011-11-395418

Seike, M., Y. Omatsu, H. Watanabe, G. Kondoh, and T. Nagasawa. 2018. Stem cell niche-specific Ebf3 maintains the bone marrow cavity. *Genes Dev.* 32:359–372. https://doi.org/10.1101/gad.311068.117

Seita, J., D. Sahoo, D.J. Rossi, D. Bhattacharya, T. Serwold, M.A. Inlay, L.I. Ehrlich, J.W. Fathman, D.L. Dill, and I.L. Weissman. 2012. Gene Expression Commons: an open platform for absolute gene expression profiling. *PLoS One.* 7:e40321. https://doi.org/10.1371/journal.pone.0040321

Stanley, E., G.J. Lieschke, D. Grail, D. Metcalf, G. Hodgson, J.A. Gall, D.W. Maher, J. Cebon, V. Sinickas, and A.R. Dunn. 1994. Granulocyte/macrophage colony-stimulating factor-deficient mice show no major perturbation of hematopoiesis but develop a characteristic pulmonary pathology. *Proc. Natl. Acad. Sci. USA.* 91:5592–5596. https://doi.org/10.1073/pnas.91.12.5592

Stier, M.T., R. Mitra, L.E. Nyhoff, K. Goleniewska, J. Zhang, M.V. Puccetti, H.C. Casanova, A.C. Seegmiller, D.C. Newcomb, P.L. Kendall, et al. 2019. IL-33 Is a Cell-Intrinsic Regulator of Fitness during Early B Cell Development. *J. Immunol.* 203:1457–1467. https://doi.org/10.4049/jimmunol.1900408

Sudo, T., T. Yokota, K. Oritani, Y. Satoh, T. Sugiyama, T. Ishida, H. Shibayama, S. Ezoe, N. Fujita, H. Tanaka, et al. 2012. The endothelial antigen ESAM monitors hematopoietic stem cell status between quiescence and self-renewal. *J. Immunol.* 189:200–210. https://doi.org/10.4049/jimmunol.1200056

Sugiyama, T., H. Kohara, M. Noda, and T. Nagasawa. 2006. Maintenance of the hematopoietic stem cell pool by CXCL12-CXCR4 chemokine signaling in bone marrow stromal cell niches. *Immunity.* 25:977–988. https://doi.org/10.1016/j.immuni.2006.10.016

Sun, J., A. Ramos, B. Chapman, J.B. Johnnidis, L. Le, Y.J. Ho, A. Klein, O. Hofmann, and F.D. Camargo. 2014. Clonal dynamics of native haematopoiesis. *Nature.* 514:322–327. https://doi.org/10.1038/nature13824

Thorens, B., J.J. Mermod, and P. Vassalli. 1987. Phagocytosis and inflammatory stimuli induce GM-CSF mRNA in macrophages through post-transcriptional regulation. *Cell.* 48:671–679. https://doi.org/10.1016/0092-8674(87)90245-5

Tikhonova, A.N., I. Dolgalev, H. Hu, K.K. Sivaraj, E. Hoxha, Á. Cuesta-Domínguez, S. Pinho, I. Akhmetzyanova, J. Gao, M. Witkowski, et al. 2019. The bone marrow microenvironment at single-cell resolution. *Nature.* 569:222–228. https://doi.org/10.1038/s41586-019-1104-8

Tomita, Y., D.H. Sachs, and M. Sykes. 1994. Myelosuppressive conditioning is required to achieve engraftment of pluripotent stem cells contained in moderate doses of syngeneic bone marrow. *Blood.* 83:939–948. https://doi.org/10.1182/blood.V83.4.939.939

Ushach, I., and A. Zlotnik. 2016. Biological role of granulocyte macrophage colony-stimulating factor (GM-CSF) and macrophage colony-stimulating factor (M-CSF) on cells of the myeloid lineage. *J. Leukoc. Biol.* 100:481–489. https://doi.org/10.1189/jlb.3RU0316-144R

Venezia, T.A., A.A. Merchant, C.A. Ramos, N.L. Whitehouse, A.S. Young, C.A. Shaw, and M.A. Goodell. 2004. Molecular signatures of proliferation and quiescence in hematopoietic stem cells. *PLoS Biol.* 2:e301. https://doi.org/10.1371/journal.pbio.0020301

Vivier, E., D. Artis, M. Colonna, A. Diefenbach, J.P. Di Santo, G. Eberl, S. Koyasu, R.M. Locksley, A.N.J. McKenzie, R.E. Mebius, et al. 2018. Innate Lymphoid Cells: 10 Years On. *Cell.* 174:1054–1066. https://doi.org/10.1016/j.cell.2018.07.017

Wilson, A., E. Laurenti, G. Oser, R.C. van der Wath, W. Blanco-Bose, M. Jaworski, S. Offner, C.F. Dunant, L. Eshkind, E. Bockamp, et al. 2008. Hematopoietic stem cells reversibly switch from dormancy to self-renewal during homeostasis and repair. *Cell.* 135:1118–1129. https://doi.org/10.1016/j.cell.2008.10.048

Yamazaki, S., H. Ema, G. Karlsson, T. Yamaguchi, H. Miyoshi, S. Shioda, M.M. Taketo, S. Karlsson, A. Iwama, and H. Nakauchi. 2011. Nonmyelinating Schwann cells maintain hematopoietic stem cell hibernation in the bone marrow niche. *Cell.* 147:1146–1158. https://doi.org/10.1016/j.cell.2011.09.053

Yu, Y., J.C. Tsang, C. Wang, S. Clare, J. Wang, X. Chen, C. Brandt, L. Kane, L.S. Campos, L. Lu, et al. 2016. Single-cell RNA-seq identifies a PD-1^{hi} ILC progenitor and defines its development pathway. *Nature.* 539:102–106. https://doi.org/10.1038/nature20105

Zhao, M., J.M. Perry, H. Marshall, A. Venkatraman, P. Qian, X.C. He, J. Ahamed, and L. Li. 2014. Megakaryocytes maintain homeostatic quiescence and promote post-injury regeneration of hematopoietic stem cells. *Nat. Med.* 20:1321–1326. https://doi.org/10.1038/nm.3706

Zhou, B.O., L. Ding, and S.J. Morrison. 2015. Hematopoietic stem and progenitor cells regulate the regeneration of their niche by secreting Angiopoietin-1. *eLife.* 4:e05521. https://doi.org/10.7554/eLife.05521

Supplemental material

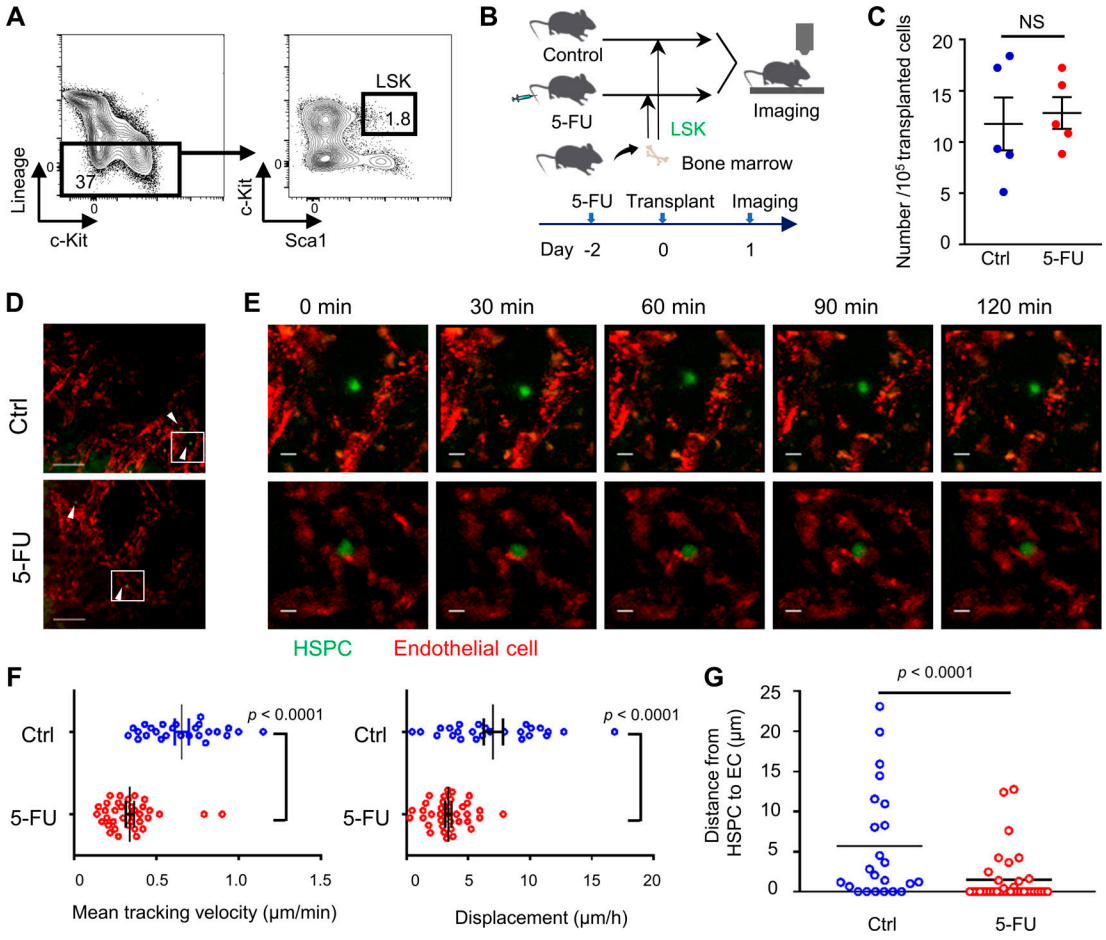

Figure S1. **Myelosuppressive BM environments influence the behavior of HSPCs. (A–G)** LSK cells, which were sorted from WT mice and labeled with green dye CMFDA, were transplanted into steady-state (control [Ctrl]) or conditioned mice treated with 5-FU 2 d before transplantation. On the day following transplantation, in vivo two-photon microscopic imaging of skull BM was performed. **(A)** Sorting strategy of LSK cells. **(B)** Schematic of the procedure. **(C)** The number of HSPCs per 10^5 transplanted cells in visualized skull bone area of control and 5-FU–treated recipient mice (n = 5 each). Results are shown as mean ± SEM. **(D)** Representative snapshots. Green (arrowhead) and red cells are HSPCs and ECs, respectively. Scale bars, 100 µm. **(E)** Magnified images from the outlined region in D. Scale bars, 10 µm. See also Video 1 and Video 2. **(F)** Three-dimensional motility of each transplanted cell was calculated. Results are shown as mean ± SEM, and each dot represents speed (µm/min) or displacement (µm/h) of an individual cell (n = 26 from seven experiments in control; n = 36 from five experiments in 5-FU). **(G)** The maximum distance from EC to each HSPC during 2-h live imaging (n = 23 from nine experiments in control; n = 36 from seven experiments in 5-FU). Results are shown as mean. Each dot represents an individual cell. Statistical significance was determined by unpaired Student's t test (C, F, and G).

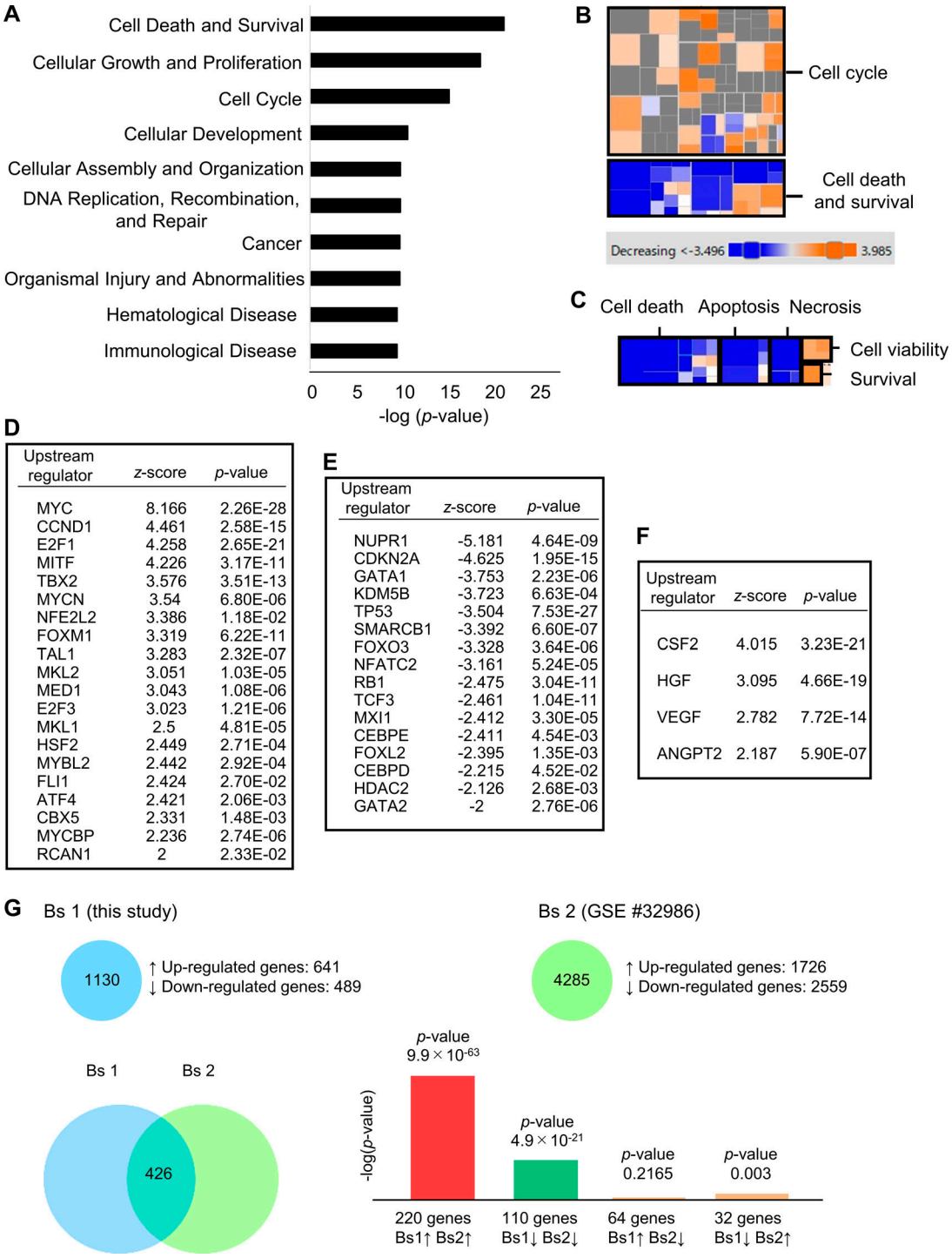

Figure S2. **Bioinformatic analysis of HSPCs homed into 5-FU–treated BM to determine activated signals. (A–F)** Bioinformatic analyses of RNA-seq data were conducted. Sequencing data shown here are overlapped with data shown in Fig. 1 C. **(A)** The top 10 enriched biological functional categories between two groups, according to the Ingenuity Knowledge Base, are listed. The x axis shows the significance, which is the value of −log(P value). **(B)** Color-coded heat map analyses regarding "cell cycle" and "cell death and survival" among enriched biological functional categories. **(C)** Subcategories in the highlighted heat map of "cell death and survival" category within B. **(D and E)** Upstream transcriptional regulators that were significantly activated (*z*-score > 2; D) or inhibited (*z*-score < −2; E) in HSPCs transplanted into 5-FU–treated mice compared with those into control mice. **(F)** Upstream cytokine/growth factors that were significantly activated (*z*-score > 2) in HSPCs transplanted into 5-FU–treated mice compared with those into control mice. **(G)** Differentially expressed genes from RNA-seq in this study (bioset 1) were compared with those in another study (bioset 2), in which gene expression of GM-CSF–stimulated versus unstimulated dendritic cells in vitro was analyzed (Min et al., 2012), using the BaseSpace Correlation Engine (Illumina). A strong positive correlation was observed between the two biosets. The Venn diagram shows the number of differentially expressed genes that are overlapped in the two biosets. The bar graph shows the significance levels of overlapped or unique genes by −log(P value). GSE, Gene Expression Omnibus Series.

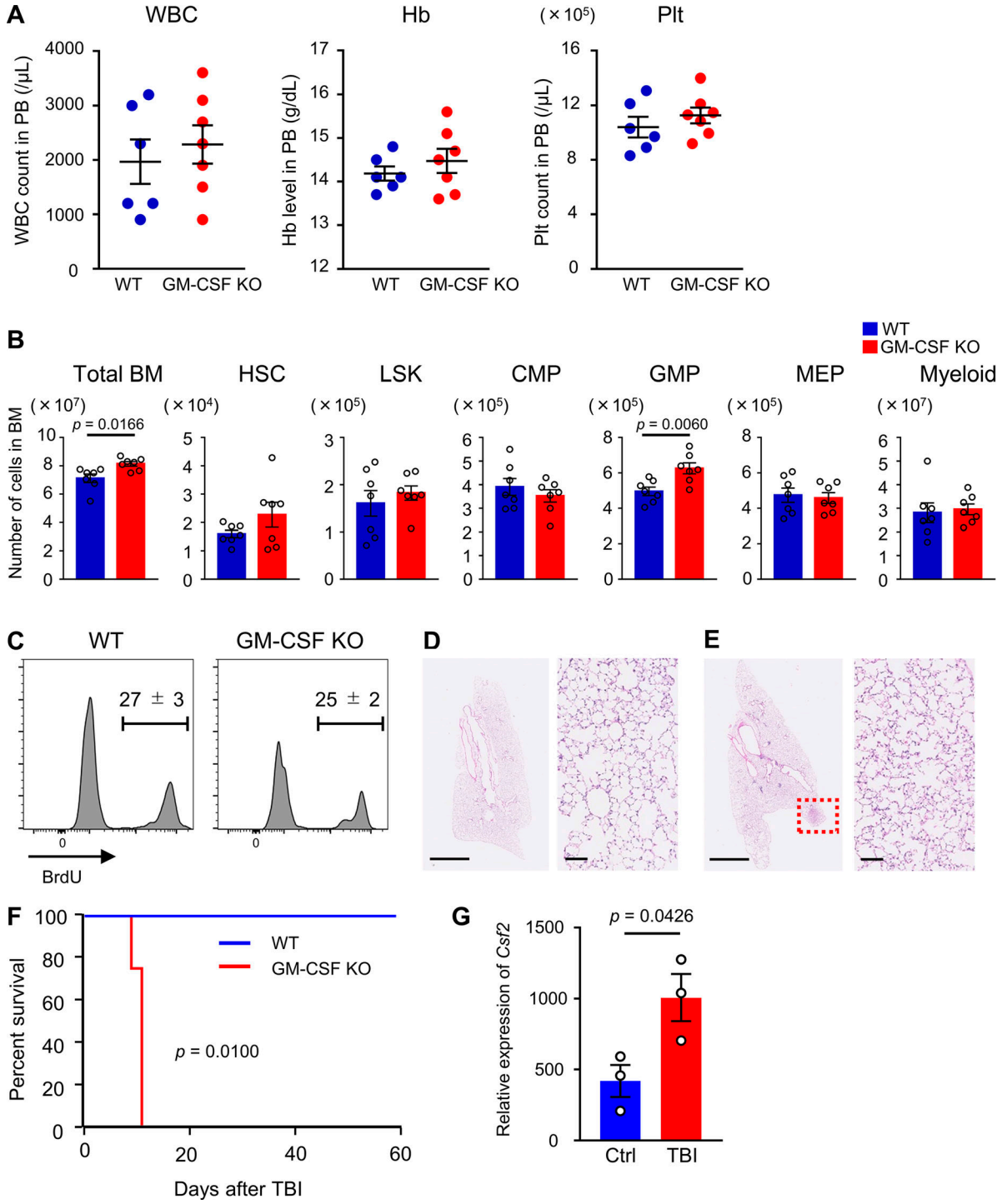

Figure S3. **Phenotype of GM-CSF–KO mice. (A and B)** PB and BM cellularity in WT and GM-CSF–KO mice in the steady-state. **(A)** WBC, hemoglobin (Hb), and platelet (Plt) counts in PB; *n* = 6 in WT, *n* = 7 in GM-CSF–KO. Data are pooled from two independent experiments. **(B)** The numbers of total BM cells, HSCs ($CD48^-CD150^+$ LSK cells), LSK cells, CMPs, GMPs, MEPs, and $Gr1^+$ or $CD11b^+$ myeloid cells from femurs and tibias; *n* = 7, pooled from two independent experiments. **(C)** BrdU incorporation in LSK cells from WT and GM-CSF–KO mice; *n* = 3, representative of two independent experiments. **(D and E)** Lung tissues from 5-FU–treated (200 mg/kg) WT and GM-CSF–KO mice at day 5 were dissected after perfusion-fixation with 4% PFA. Dissected tissues were further fixed in 4% PFA overnight and embedded in paraffin. Sections from WT (D) and GM-CSF–KO (E) mice stained with hematoxylin and eosin are shown. Scale bars, 2.5 mm in left panels, 100 μm in right panels. Dotted red square in E shows tubercule composed of eosinophilic protein. **(F)** Kaplan–Meier survival curves of WT (blue line) or GM-CSF–KO mice (red line) that received 5.5 Gy of TBI; *n* = 4, representative of two independent experiments. **(G)** qRT-PCR analyses for the expression of *Csf2* in WT ILC2s from control (Ctrl) or TBI (5.5 Gy) day 2 mice; *n* = 3, representative of two independent experiments. In the bar charts, the results are shown as mean ± SEM, and each dot represents an individual mouse. Statistical significance was determined by unpaired Student's *t* test (A–C and G) or log-rank test (F).

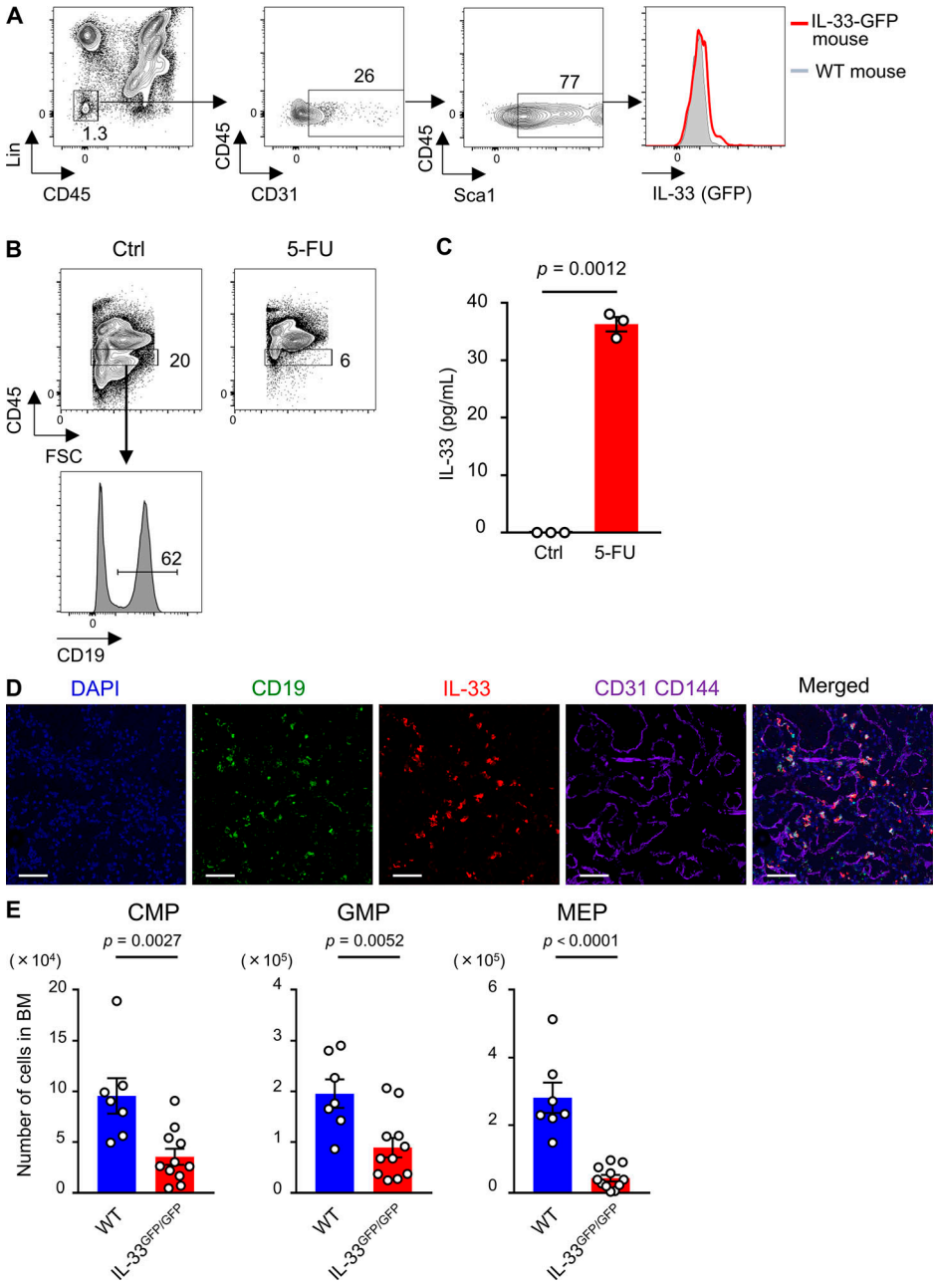

Figure S4. **B cell progenitors are a source of IL-33 in injured BM. (A)** Flow cytometry of collagenase-treated BM samples from IL-33–GFP mice. In the histogram, IL-33–GFP levels in Lin⁻CD45⁻CD31⁺Sca1⁺ ECs of IL-33–GFP (red line) and control (Ctrl) WT (gray-tinted line) mice are shown. Results shown are representative of three independent experiments. **(B)** Flow cytometry of flushed BM cells from WT mice on day 0 (Ctrl) and day 2 after 200 mg/kg 5-FU injection. In upper panels, gated fraction represents $CD45^{Lo}$ BM cell. Lower histogram shows the expression level of CD19 in $CD45^{Lo}$ cells of homeostatic WT mice. Results shown are representative of three independent experiments. **(C)** CD19⁺ B cells from BM of WT mice were seeded in the presence of 5-FU. IL-33 levels of supernatants and control culture medium were measured by ELISA; $n = 3$, representative of two independent experiments. **(D)** Immunohistochemical analyses of BM sections from 5-FU–treated mice (200 mg/kg, day 2). Scale bars, 50 µm. Results shown are representative of two independent experiments. **(E)** WT and $IL\text{-}33^{GFP/GFP}$ mice were treated with 150 mg/kg 5-FU. BM cellularity was analyzed on day 8. The numbers of CMPs, GMPs, and MEPs from femurs and tibias are shown; $n = 7$ in WT, $n = 11$ in $IL\text{-}33^{GFP/GFP}$. Data are pooled from two independent experiments. In the bar charts, the results are shown as mean ± SEM, and each dot represents an individual mouse. Statistical significance was determined by unpaired Student's *t* test (C and E).

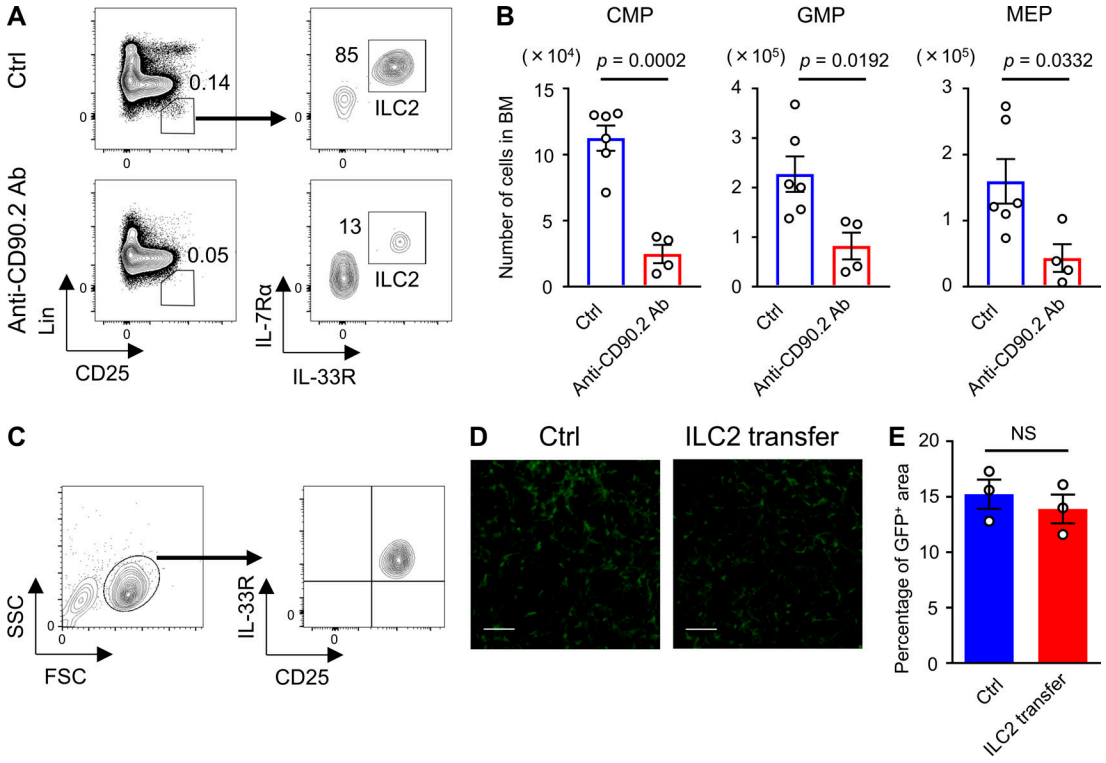

Figure S5. **ILC2s are responsible for hematopoietic recovery. (A)** Flow cytometry plots of BM cells from control (Ctrl) or anti-CD90.2 Ab-treated WT mice. Mice received four injections of 200 µg anti-CD90.2 Ab intraperitoneally every other day until 1 d before being euthanized. Control mice were injected with PBS. Results shown are representative of three independent experiments. **(B)** Control and anti-CD90.2 Ab-treated WT mice were injected with 150 mg/kg 5-FU. BM cellularity was analyzed on day 8 after 5-FU treatment. CMP, GMP, and MEP numbers from femurs and tibias; $n = 6$ in controls, $n = 4$ in Ab-treated mice. Results shown are representative of two independent experiments. **(C)** Flow cytometry plots of cultured ILC2s. Results shown are representative of three independent experiments. **(D and E)** CXCL12-GFP mice were treated with 150 mg/kg 5-FU, and whole-mount confocal microscopy BM analysis was performed on day 7. In the ILC2 transfer group, mice were transferred with 2×10^5 ILC2s from WT mice on days 1 and 2. Control mice were injected with PBS. **(D)** Representative MIP images of the CXCL12-GFP mice femoral bones. Green, CAR cells. Scale bars, 50 µm. **(E)** CXCL12-GFP$^+$ area fractions relative to the whole visual field; $n = 3$, representative of two independent experiments. In the bar charts, the results are shown as mean ± SEM, and each dot represents an individual mouse. Statistical significance was determined by unpaired Student's *t* test (B and E).

Video 1. **Time-lapse video of skull BM of a steady-state mouse transplanted with HSPCs.** Green, HSPCs. Red, ECs. The playback speed is 12 frames per second. (Actively moving red cells are considered to be macrophages.)

Video 2. **Time-lapse video of skull BM of a 5-FU–treated mouse transplanted with HSPCs.** Green, HSPCs. Red, ECs. The playback speed is 12 frames per second. (Actively moving red cells are considered to be macrophages.)

Three tables are provided online as separate Excel files. Table S1 lists the 10 most highly expressed genes in ILC2 cluster cells compared with cells from other clusters. Table S2 lists the six genes most highly co-expressed with *Csf2*. Table S3 lists the Abs used in this study.